High current transport experiment for heavy ion inertial fusion

L. R. Prost, P. A. Seidl, F. M. Bieniosek, C. M. Celata, A. Faltens, D. Baca, E. Henestroza, J. W. Kwan, M. Leitner, and W. L. Waldron
Lawrence Berkeley National Laboratory, Berkeley, California 94720, USA

R. Cohen, A. Friedman, D. Grote, S. M. Lund, and A. W. Molvik
Lawrence Livermore National Laboratory, Livermore, California 94550, USA

E. Morse
University of California, Berkeley, California 94720, USA
(Received 18 June 2004; published 21 February 2005)

The High Current Experiment at Lawrence Berkeley National Laboratory is part of the U.S. program to explore heavy-ion beam transport at a scale representative of the low-energy end of an induction linac driver for fusion energy production. The primary mission of this experiment is to investigate aperture fill factors acceptable for the transport of space-charge-dominated heavy-ion beams at high intensity (line charge density $\sim 0.2\ \mu\mathrm{C/m}$) over long pulse durations (4 μs) in alternating gradient focusing lattices of electrostatic or magnetic quadrupoles. This experiment is testing transport issues resulting from nonlinear space-charge effects and collective modes, beam centroid alignment and steering, envelope matching, image charges and focusing field nonlinearities, halo, and electron and gas cloud effects. We present the results for a coasting 1 MeV K^+ ion beam transported through ten electrostatic quadrupoles. The measurements cover two different fill factor studies (60% and 80% of the clear aperture radius) for which the transverse phase space of the beam was characterized in detail, along with beam energy measurements and the first halo measurements. Electrostatic quadrupole transport at high beam fill factor ($\approx 80\%$) is achieved with acceptable emittance growth and beam loss, even though the initial beam distribution is not ideal (but the emittance is low) nor in thermal equilibrium. We achieved good envelope control, and rematching may only be needed every ten lattice periods (at 80% fill factor) in a longer lattice of similar design. We also show that understanding and controlling the time dependence of the envelope parameters is critical to achieving high fill factors, notably because of the injector and matching section dynamics.

DOI: 10.1103/PhysRevSTAB.8.020101 PACS numbers: 52.58.Hm, 52.59.Sa, 41.75.Ak, 41.85.Ne

I. INTRODUCTION

The High Current Experiment (HCX) [1], located at Lawrence Berkeley National Lab and carried out by the Heavy-Ion Fusion Virtual National Laboratory (HIF-VNL),[1] is designed to explore the physics of intense beams in the context of developing a heavy-ion high-intensity accelerator (i.e., driver) for an inertial fusion power plant [2,3].

At an injection energy of 1–1.8 MeV, a line-charge density, λ, of 0.1–0.2 $\mu\mathrm{C\,m^{-1}}$, and a pulse duration of 4 μs, the HCX main beam parameters are in the range of interest for a fusion driver front end. At 1 MeV, where we performed our experiments, the generalized beam perveance is

$$K = \frac{2qI_B}{4\pi\varepsilon_0 m(\beta\gamma c)^3} = 8 \times 10^{-4}, \qquad (1)$$

and the tune depression, defined as the ratio of the single-particle oscillation response to the applied focusing fields with and without the space-charge potential, is 0.2. In this regime space-charge forces strongly influence the beam properties during its transport, and image charges induced on metallic structures of the machine aperture play an important role. For comparison, the beam line-charge density and generalized perveance of large accelerator facilities such as the Spallation Neutron Source (SNS) Front End [4–6] and Fermilab's Linac Experimental Facility [7–9] are 1 to 2 orders of magnitude lower than the HCX parameters. Also, in both cases, the beam is rapidly accelerated to energies where space-charge effects are diminished. For heavy-ion inertial fusion, where the line-charge density increases from $\approx 0.2\ \mu\mathrm{C\,m^{-1}}$ at injection to $\approx 1.7\ \mu\mathrm{C\,m^{-1}}$ at the end of the accelerator (4.0 GeV, Bi^+) and approximately $30\ \mu\mathrm{C\,m^{-1}}$ at the end of the drift compression at the *D-T* target [10], the perveance is increased by beam bunch compression as part of the acceleration schedule, which optimizes the induction linear accelerator efficiency.

Previous scaled experiments at LBNL [11–14] were designed with the appropriate perveance for studying driv-

[1]The Heavy-Ion Fusion Virtual National Laboratory is a collaboration between groups at LBNL, LLNL, and Princeton Plasma Physics Laboratory, pursuing the common beam science for high energy density physics and inertial fusion energy.

erlike phenomena, principally transport with sufficient current to highly depress the single-particle betatron tunes, but the beam current was kept relatively low. For example, in the Single Beam Transport Experiment [15], the maximum generalized perveance was 2.2×10^{-3}—higher than generally envisioned for a fusion driver—but the line-charge density remained about 1 order of magnitude lower than for the HCX or a fusion driver front end. The University of Maryland Electron Ring [16], which was designed for studying the transport of high-intensity electron beams in a strong focusing lattice, can also produce highly tune-depressed beams with a line-charge density of $\lambda \approx 1.5 \times 10^{-3}\ \mu\mathrm{C\,m^{-1}}$ [17].

A principal goal of the HCX experiment is to evaluate the maximum acceptable beam fill factor, i.e., the maximum radial extent of the beam within the physical aperture (i.e., $r_{\mathrm{beam}}/r_{\mathrm{bore}}$, where r_{beam} is the maximum envelope excursion [2 root-mean-square (RMS)] of a beam propagating in a transport channel of radius r_{bore}, which is the physical clear bore radius inside the quadrupoles), addressing the question of how compact a multiple-beam focusing lattice can be to accommodate the transport and acceleration of the heavy-ion beams. Higher fill factors are desirable because they make more economically efficient use of material structures. For example, cost savings of 50% have been projected in multibeam drivers if the fill factor can be increased from 60% to 80% [18]. The fill factor study in this experiment addresses the more fundamental issue of how much charge can be transported in a single channel without beam loss or deterioration of the beam quality. Greater fill factors enhance nonideal physics effects resulting from imperfect focusing optics, image charge and halo impacting material structures and releasing desorbed gases that interact with long-pulse beams, creating possible electron-cloud effects. These are intense beam physics issues that may be relevant to other accelerator applications requiring high intensity, such as spallation neutron sources and the production of rare isotopes. Design and engineering issues such as the frequency at which the beam coherent oscillation (i.e., centroid) must be corrected for, or the alignment tolerances for the focusing elements, are also less favorable the greater the fill factor and are also addressed.

The HCX beam transport line is at present mainly based on an alternating gradient (AG) electrostatic quadrupole focusing (i.e., quadrupoles with equal voltages alternating in sign), which provides efficient transport at low energy. Secondary electrons are expected to be swept out of the beam path by the quadrupole fields and are not anticipated to set transport limits. In follow-up experiments, transport-limiting effects in magnetic quadrupoles due to electrons are being explored. In that situation, electrons can be trapped by the beam self-potential and disrupt the beam dynamics.

The organization of this paper is as follows: In Sec. II we present the apparatus including the diagnostics, in Secs. III and IV we show beam measurements from the injector and the matching section, in Sec. V we discuss the beam current time dependence and the consequences on the beam envelope and beam control, in Sec. VI we show the fill factor results for the transport through electrostatic quadrupoles, in Sec. VII we discuss the features of the measured beam charge distribution, in Sec. VIII we present the beam energy measurements, and in Sec. IX we discuss the main results of our experiments. Conclusions and implications for future heavy-ion accelerators are in Sec. X.

II. EXPERIMENTAL CONFIGURATION

The present configuration consists of the K^+ ion source and injector, an electrostatic quadrupole matching section (six quadrupoles), ten electrostatic transport quadrupoles, and four room-temperature (RT) pulsed magnetic quadrupoles. A multipurpose diagnostic station (D end) is at the end of the beam line (Fig. 1). This paper discusses the results from the electrostatic transport section.

A. Injector

The injector consists of a 10.0-cm diameter hot surface ionization source assembly followed by a 750 kV extraction diode, then by four electrostatic quadrupoles (ESQs) biased to focus the beam transversely while accelerating longitudinally (up to 2 MV) [19,20]. Figure 2 shows the source assembly, the gate electrode that provides the extraction and the ESQ column.

The injector is contained inside a pressure vessel, filled with a high-voltage insulating gas mixture (90% N_2 and 10% SF_6). The vessel houses 38 stages of a two-section network Marx generator, which produces a flattop voltage pulse (V_{Marx}) and a high-voltage ''dome'' containing the source and extraction pulse electronics. The high-voltage dome also houses a hydraulically driven 400 Hz, 10 kVA alternator which powers all the source electronics, including the telemetry system. Voltages to the various electrodes of the diode and accelerating column are obtained from a sodium sulfate solution water resistor (i.e., water resistor, $R \approx 5\ \mathrm{k}\Omega$). The source is biased at a negative dc potential (V_{bias}) while the gate electrode is tied to the potential of the dome, inhibiting ion emission from the hot surface. During ion extraction, the extraction circuit, which controls most of the emission, delivers a pulse swing (V_{gate}) up to 140 kV, going from a bias voltage of -60 kV to an extraction voltage of $+80$ kV, applied to the source with respect to the gate electrode through a step-up transformer driven by a tunable pulse forming network [21,22]. Note that the source filament transformer not only supplies the heater power (2.5 kW), but is also a high-voltage isolation transformer allowing the source to be biased at up to -80 kV. Trigger, timing, and diagnostics information are transmitted to and from the high-voltage dome by analog fiber optics links.

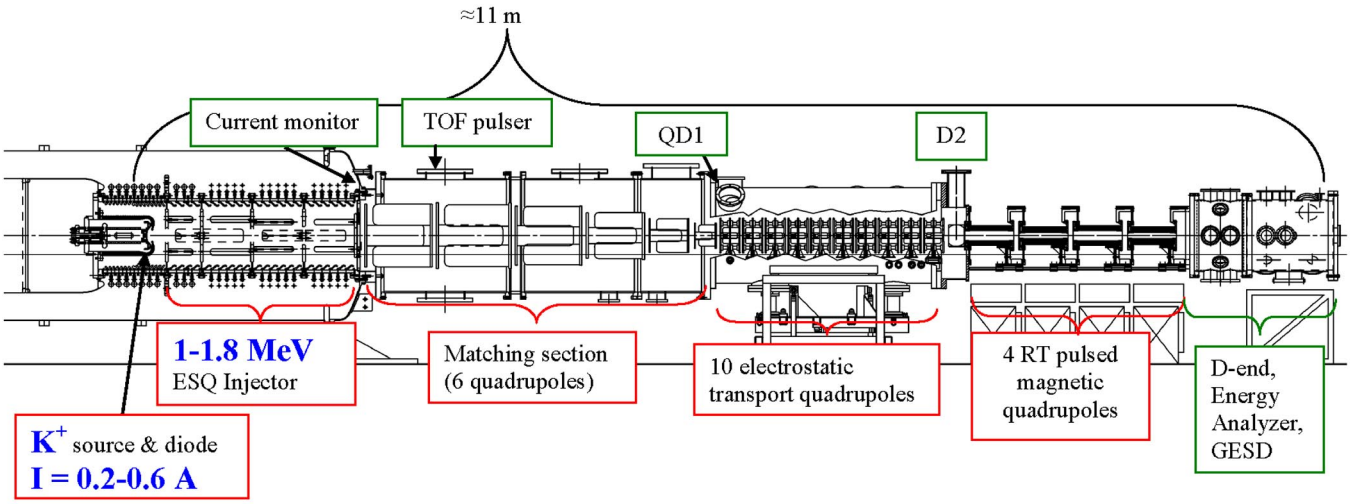

FIG. 1. (Color) Layout of the HCX (elevation view).

Figure 3 shows the Marx pulse and the gate pulse with their respective timings. The gate pulse length is 4.5 μs flattop. Over that time, the Marx pulse is flat to within 1.4%. The repetition rate is 0.1 Hz at 1 MeV.

The Marx voltage drifts due to changes in the conductivity of the water resistor. We keep the peak beam energy (E_B) within $\pm 0.5\%$ of its nominal value by monitoring the Marx voltage pulse output with a capacitive probe and

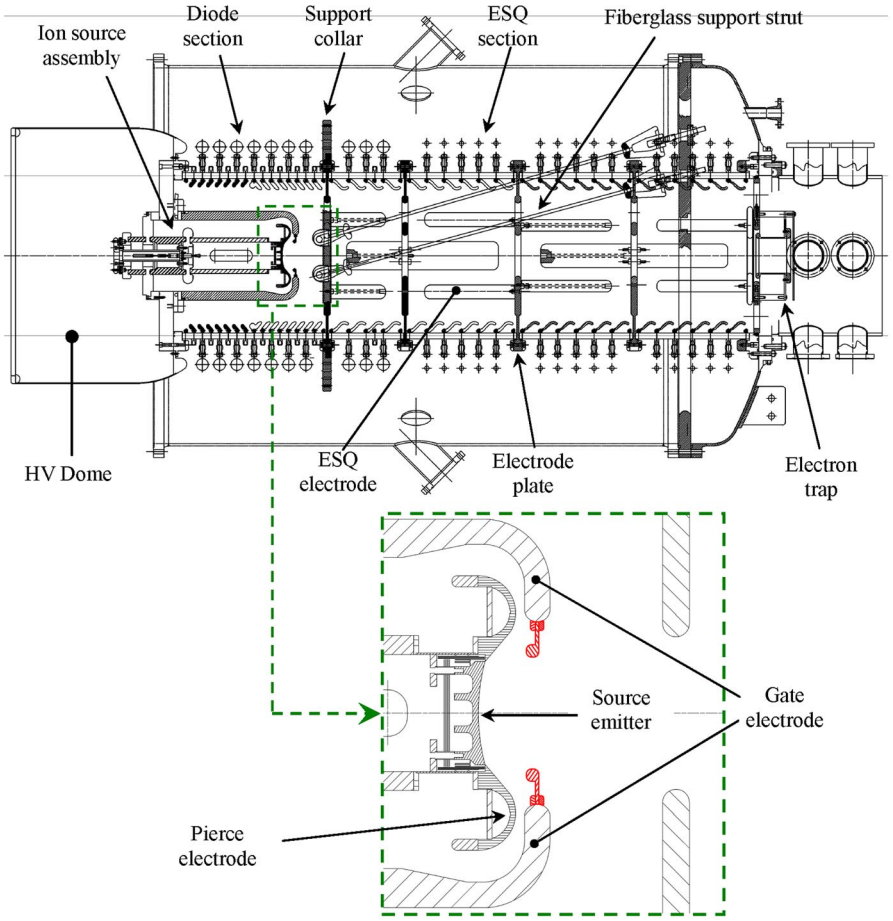

FIG. 2. (Color) 2-MV injector accelerator column showing fiberglass support struts. The column length is 2.4 m. The red part in the inset shows the addition to the gate electrode reducing its aperture diameter from 179.5 to 110 mm.

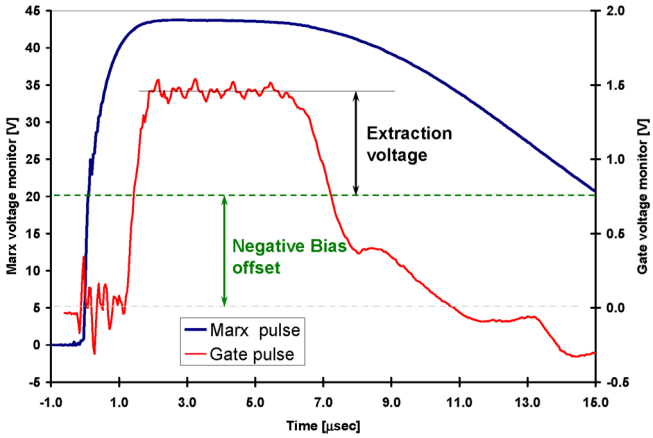

FIG. 3. (Color) Typical Marx (blue) and gate (red) pulses. The Marx pulse is viewed through a capacitive monitor, whose gain is 21.4 kV/V. The gate pulse is viewed through a resistive divider and an optical link. In green we show the negative dc bias that is applied to the source. Note that the ripples seen on the gate voltage early and during the flattop of the pulse are due to electrical noise picked up on the cables when the trigger chassis of the Marx column fires.

adjusting the Marx charging power supplies set point accordingly. Moreover, the beam current (I_B) also drifts by several percent if left uncorrected during an ~8 h period. This drift is attributed to electronics and possibly material effects in the source. Therefore, beam parameters are also kept constant by empirically adjusting the charge voltage of the gate electrode pulser to maintain a constant averaged beam current.

At beam energies higher than ~1.5 MeV, operation is complicated by the fact that the water resistor partially deforms under the higher required dome pressure load, affecting the voltage division along the accelerating column and modifying the injector optics [22].

B. Matching section

The matching section (Fig. 4) consists of six electrostatic quadrupoles (QM1–QM6) designed to compress the beam area transversely by a factor ≈ 25 and produce the matched beam parameters for transport in the periodic electrostatic lattice.

The radii of the first (QM1) and last (QM6) matching quadrupole bores are $r_{\mathrm{bore}} = 100$ and 31 mm, respectively. Each quadrupole is independently energized and the power supplies are remotely controlled and monitored via Ethernet links. Matching quadrupole voltages range up to ± 43 kV for $E_B = 1.0$ MeV, and focusing gradients up to 9 kV/cm^2 are produced by the lattice (quadrupole potentials scale linearly with the beam energy).

Residual misalignment of the source in the diode region, nonuniformities in the source's current density distribution, and alignment of the focusing elements of the injector and matching section drive betatron oscillations of the beam centroid through the quadrupoles of the matching section. QM4–6 may each be moved in the horizontal and vertical directions by up to ± 15 mm to correct the beam centroid offset.

C. Electrostatic transport section

The transport section consists of ten electrostatic quadrupoles on a common supporting rail (Fig. 5). The quadrupoles are aligned to within ± 100 μm on the bench before installation inside the vacuum tank.

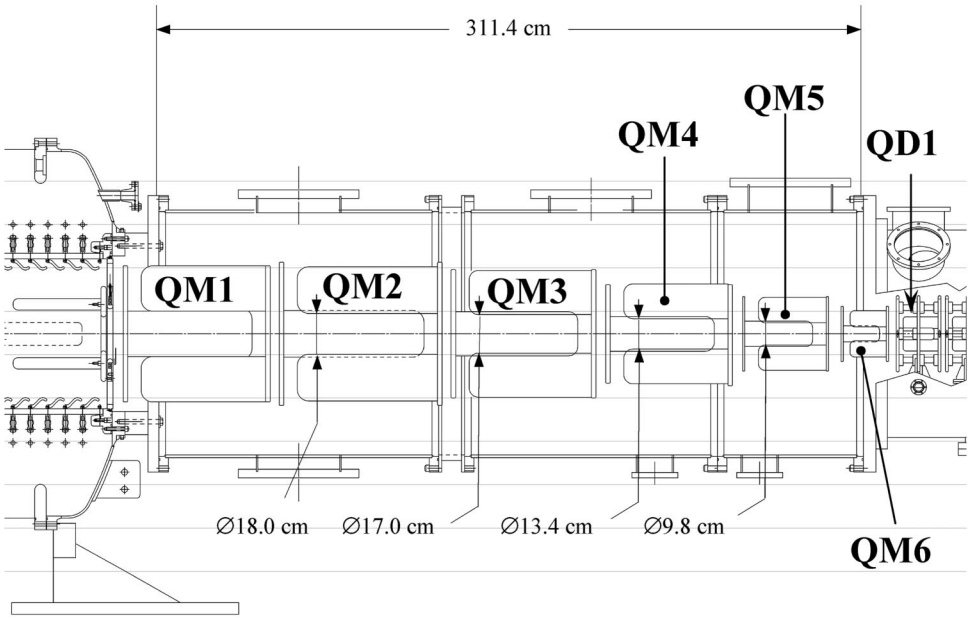

FIG. 4. Mechanical drawing (elevation view) of the matching section. On the left is the injector. On the right is the first quadrupole of the transport section (QD1) which is movable to allow room for diagnostics.

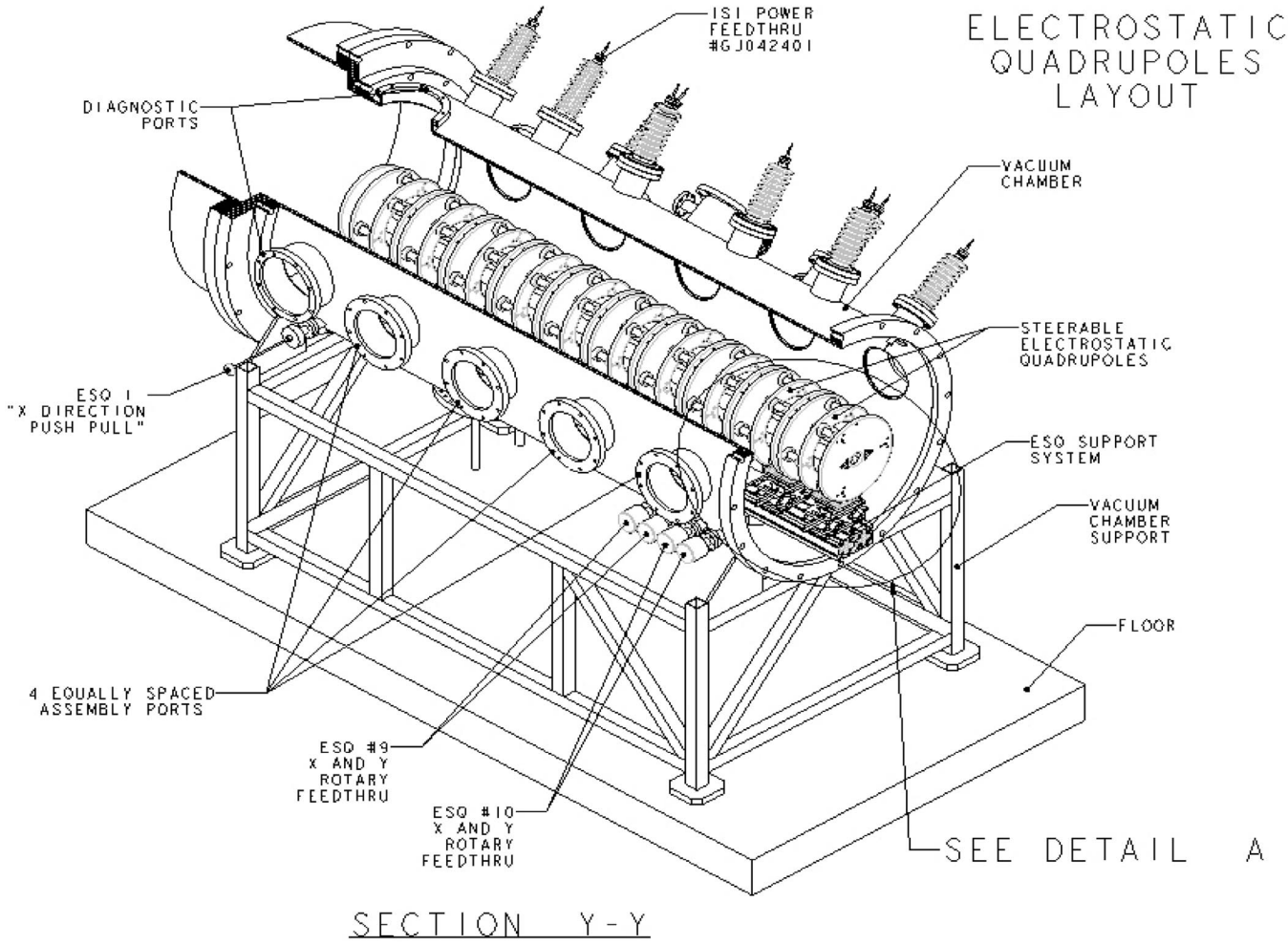

FIG. 5. Cutaway view of the electrostatic transport section.

The rail is mounted on a six-strut/kinematic system, with alignment fiducials outside the vacuum chamber, decoupling it from the vacuum tank. It is then aligned independently to the rest of the beam line. The first quadrupole (QD1) is movable, allowing insertion in its place of various diagnostics to measure the beam properties before transport. The last two quadrupoles (QI9 and QI10) may be displaced (horizontal and vertical directions) to correct betatron centroid oscillations. Additionally, QD1 can be rotated by two or four degrees for studying the effect of rotated quadrupoles on the beam. QD1 and QI7 to QI10 are independently biased. The second to sixth quadrupoles (Q2 to Q6) are energized in parallel. For QI7 to QI10, each feedthrough supplies independent voltages to adjacent quadrupoles, preventing a voltage differential larger than 20 kV between QI7 and QI8, and QI9 and QI10. All power supplies are remotely controlled and monitored via Ethernet links. Figure 6 shows the adopted quadrupole design. They are operated bipolar, and prototypes have held voltages up to ± 120 kV (in absence of beam), twice their maximum operating voltage.

The bore radius of the quadrupole channel is $r_{\text{bore}} = 2.3$ cm. The electrodes are cylindrical (as in a multibeam array) and follow $r_{\text{electrode}} = (8/7)r_{\text{bore}}$ to minimize the sum of higher order multipoles. The drift length between two quadrupole end plates is 2 cm and the half-lattice period $L = 217.6$ mm. A calculation of the electrostatic field based on the mechanical design showed very good field quality with integrated higher order multipoles equal to 0.73% of the integrated quadrupole component at a radius $r = 2$ cm from the center of the quadrupole, down to 0.24% at $r = 1.5$ cm and 0.06% at $r = 1$ cm. The effective length of the quadrupole moment $E_{Qr}(z)$, defined as $l_{\text{eff}} = [\int E_{Qr}(z)dz]/E_{Qr}(z = 0)$, where $z = 0$ is the center of the quadrupole, is 151.5 mm. The lattice longitudinal occupancy (i.e., l_{eff}/L) is $\eta = 0.70$.

D. Diagnostics

Beam diagnostics are located at the interface of the matching section and the ten transport quadrupoles section (QD1), after the last transport quadrupole in the periodic

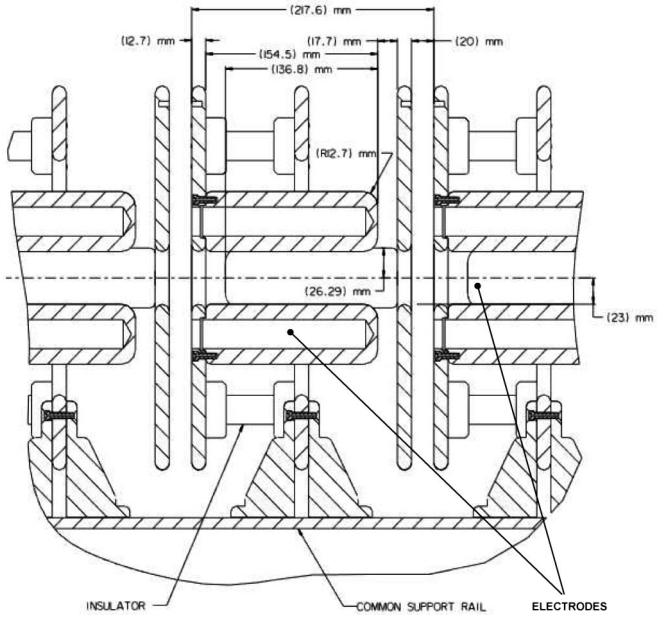

FIG. 6. Mechanical drawing (side view) of a quadrupole installed on the beam line.

lattice (D2) and at the end of the beam line (D end) (see Fig. 1). At the early stages of the experiment, the apparatus did not include the D2 diagnostics station and the magnetic quadrupoles. Instead, the electrostatic lattice was directly coupled to the D-end diagnostics tank. The z locations of the D2 phase-space measuring planes since March 2003 are 5.5 cm (horizontal) and 8.6 cm (vertical) upstream of the D-end measuring planes prior to March 2003. Note that all data taken at the exit of the electrostatic transport section (''D-end data'' before March 2003; ''D2 data'' after March 2003) will be referred to as D2 data, unless otherwise specified.

When making measurements at QD1, the first quadrupole of the electrostatic transport section is moved out of the beam path via a vacuum feedthrough and lead screw assembly, and the selected diagnostics are moved in. There is no quadrupole at D2, so that after QI10 there is a drift of 15.2 cm to the first magnetic quadrupole. All diagnostics stations include transverse slit scanners and Faraday cups (with an additional current transformer at QD1). A large current transformer at the exit of the injector monitors the total beam current. The total current measurements are accurate to $\pm 1\%$.

Transverse slit scanners consist of pairs of paddles (moving horizontally and/or vertically) holding stainless steel slits and slit-cups (i.e., a compact assembly composed of a shallow Faraday cup or simple collector plate located behind a masking slit). Each paddle is independently driven by a computer-controlled step motor, with a positioning accuracy of ≈ 10 μm. The step motors reside outside the vacuum system and drive the diagnostic slit (or slit-cup) via a ferrofluidic seal and lead screw assembly. Depending on the diagnostic station, slits are 25 or 50 μm wide and 7 to 20 cm long. Slit-cups are biased such that secondary electrons amplify the collected incident ion signal by a factor of ≈ 40.

Stepping through the beam with a slit-cup gives a transverse current density profile. This measurement integrates over the current density in the plane perpendicular to the motion of the slit-cup. For instance, for a horizontal profile (x direction), where the slit is oriented vertically (y direction), the measured signal is proportional to

$$\rho(x, t) = \int J(x, y, t) dy,$$

and similarly in the other (y) direction, where $J(x, y, t)$ is the beam current density as a function of time. These measurements determine the beam centroid and radius in one of the transverse planes. They also indicate large-scale asymmetries or distortions of the distribution from ''ideal'' uniform density elliptical cross sections. The signal-to-noise ratio for profile measurements ranges from 15:1 to 500:1 depending on the slit width and the current density at the location of the measurement.

The projected phase-space distribution of the beam [$f(x, x', t)$ or $f(y, y', t)$] is measured with a slit and a parallel slit-cup. The slit is located 10–15 cm upstream of the slit-cup and determines the position coordinate, x or y, of the beam being sampled. The slit-cup is then scanned through the transmitted slice to measure the transverse velocity distribution (x' or y') at that position. The drift distance between the slit and the slit-cup is chosen such that $<1\%$ of the measured transverse envelope expansion of the transmitted slice is due to the remaining space-charge forces. This procedure is repeated to map phase-space density projections [13,15,23]. The signal-to-noise ratio varies from 10:1 to 300:1 depending on the diagnostic station and the current density at the collector.

A slit and slit-cup pair oriented perpendicular to each other is used to map out the current density distribution in the plane perpendicular to the beam motion, $J(x, y, t)$ [23]. The upstream slit determines one position coordinate, x or y, and the slit-cup the other, y or x. The difference between this and the phase-space measurements described above is that the downstream slit is scanning through the long dimension of the transmitted sheet beam. This is illustrated in Fig. 7. This results in a smaller signal amplitude, but the high-intensity beam allows this procedure to be carried out with good signal-to-noise ratio (≈ 15:1). A Kapton film was also used to produce time-integrated images of the beam [24]. Kapton is an organic polymer that degrades when exposed to the beam. This degradation results in a darkening of the film, which indicates the time-integrated beam current distribution. Kapton has linear dose response over the range of interest and excellent spatial resolution. It also discriminates against low energy and low mass particles (e.g., electrons).

All these measurements (except for the Kapton image) are time resolved with a typical resolution of 40 to 120 ns.

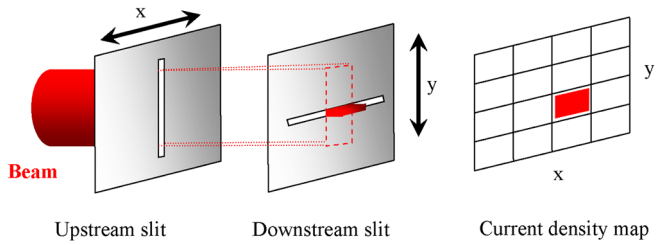

FIG. 7. (Color) Schematic illustrating the current density mapping procedure.

The minimum time resolution is of the order of 10 ns, limited by the transit time of the ions through the slit-cup detector and the capacitance of the circuit (including the collector). They rely on the beam properties being both reproducible from shot to shot and also over long periods of time. Forty to 275 pulses are required for transverse profile and phase-space measurements, and 3500–4000 for the full current density distribution. The stability of the injector is adequate and will be addressed in a later section. The power supplies that energize the quadrupoles of the matching and transport sections are stable to $\pm 0.1\%$. Shot-to-shot variations in beam current, I_B, and beam energy, E_B, contribute to overall uncertainties, which are folded into the evaluation of the uncertainties of the envelope parameters and emittance.

All data collected with the mechanical slit scanners are analyzed with routines written in MATLAB^{TM} [25]. These routines allow quick manipulation of the data such as background subtraction and extraction of the first and second moments of the beam distribution used in the calculation of the emittance. Various plots are also generated, including phase-space diagrams as a function of time. Signals with less than 2%–6% of the peak amplitude are rejected for the calculation of the moments, depending on the diagnostics station. The statistical beam envelope radii and angles (a, a', b, b') are defined in the appendix.

The last two of four quadrupole magnets are being instrumented with diagnostics specifically designed to explore beam-gas and electron-cloud issues (e.g., flush probes, gridded probes, ion and electron energy analyzers) [26].

A gas and electron source diagnostic (GESD) [26] is located at the end of the diagnostics tank (D end) and is used to measure electron emission and gas desorption yields from ions incident on targets near grazing incidence ion angle. These data are intended for calibration of the signal intensities collected on the flush-probe electrodes in the magnetic quadrupoles so that the beam loss and the gas desorption rate may be inferred. The GESD can also be used to study mitigation techniques for such undesirable effects.

The GESD can be removed and replaced with an electrostatic energy analyzer (EA). The EA is used for direct beam kinetic energy measurements but also provides time-dependent longitudinal phase-space information. The EA, a 90° spectrometer with a radius of 46 cm, and a gap between the two electrodes of 2.5 cm, was operated up to $\Delta V = 110$ kV, corresponding to a beam energy of 0.9 MeV. The relative accuracy is $\pm 0.2\%$, allowing detection of small energy variations as a function of time during the beam pulse. The absolute calibration depends on the geometry and fringe fields of the analyzer. By changing the beam energy by a known absolute amount, we were able to provide an independent calibration: The beam passed through a 28%-transparent hole plate, and the gas cloud created at the biased hole plate stripped some singly charged K^+ beam ions to doubly charged K^{2+}, which were detected in the analyzer. Thus, the absolute beam mean energy is measured to $\pm 2\%$.

Beam energy measurements can also routinely be done by a time-of-flight (TOF) technique. A fast pulser in the matching section (0.3 μs FWHM) induced 1% energy perturbations near the middle of the beam pulse. These energy pulses manifest as 5%–10% current perturbations when measured 5.4 m downstream. They have been used as a time stamp for an accurate determination of the time of flight of the particles. The TOF measurements are accurate to $\pm 2\%$. This is more accurate than, for example, measuring the TOF by detection of the arrival time of a current equal to 50% of the maximum of the beam rise time because the longitudinal space charge of the beam at the head (and tail) modify the longitudinal distribution and measured arrival times

Additionally, a prototype optical diagnostic [27] is installed in the D-end tank and a more compact optical diagnostic subsequently developed is installed at D2. They consist of movable slits (x or y direction) that intercept the beam, and a thin sheet of scintillator material placed in the path of the transmitted sheet beam. The light resulting from the ions interacting with the scintillator material is then captured through an optical window with a gated charge-coupled device camera located outside the vacuum chamber [27]. The function of the optical diagnostic is equivalent to the slit scanner described above with the additional advantage of providing additional information about the 4D beam distribution [i.e., $f(x, y', t)$ and $f(y, x', t)$] rather than integrated slit projection, because intensity along the slit is also measured. Used with an ensemble of pinholes, it would measure the full transverse 4D distribution. They also allow for a much faster data acquisition time for equivalent spatial and angular resolution. The light intensity distribution is later analyzed to derive the second moments and emittance of the beam. These images are also compiled to give a $J(x, y)$ distribution of the beam. Though it is possible to image the whole beam directly onto the scintillator to get its transverse current density distribution in a single pulse, the light output of the scintillator material degrades under high-intensity bombardment.

Finally, all of the electrostatic quadrupoles are biased through coupling circuits, allowing them to act as capacitive pickups and beam loss monitors when the beam passes. When in a quadrupole, the beam induces image charges onto the electrodes. As the charge subtended by the quadrupole electrodes builds up (or decreases), a current flows through the coupling circuit and a voltage drop appears across the resistor R_{monitor} such that we can measure

$$V(t) = R_{\text{monitor}} \frac{dQ_0(t)}{dt}, \tag{2}$$

where $Q_0(t)$ is the total charge within the quadrupole at time t and is proportional to the beam current I_B. For a trapezoidal current pulse (square pulse with linear rise and fall times), the resulting capacitive pickup signal is a positive and negative peak separated by the beam duration. Secondary particles (ions and electrons) resulting from direct interaction with the electrodes will travel from one electrode to another (of the opposite polarity). Since electrodes are biased in pairs and monitored through the same coupling circuit, this displacement of charges induces a current that will be measured in addition to the capacitive effect. In particular, the collection of lost ions and emission of secondary electrons during the ''flattop'' of the beam pulse generates a signal (negative for positively biased electrode pairs and positive for negatively biased electrode pairs) proportional to the beam losses. The pickup signal due to lost ions is amplified by the large secondary electron coefficient (a parametric fit from data taken from 80° to 88° gives $\gamma_e \cong 7\cos^{-1}\theta$, where $\theta = 0°$ indicates normal incidence to the surface [26]; typical angles of lost ions are expected to be near grazing where γ_e is maximal), making this diagnostic more sensitive to beam loss than comparisons of the total beam current data at different locations along the beam line. They additionally indicate regions of the lattice where envelope excursions and centroid offsets cause particle loss from scraping. However, since the collected signal is directly proportional to γ_e, which depends on the angle of incidence of the ions on the electrodes, the uncertainty on the absolute value of the current loss is large. For interpretation of the pickup signals, an effective secondary electron yield $50 < \tilde{\gamma}_e < 100$ is assumed. Viewed through $R_{\text{monitor}} = 10\ \Omega$, a pickup signal amplitude of 1 V corresponds to $1 < I_{B\ \text{loss}} < 2$ mA.

At a pressure of 10^{-7} Torr, beam loss due to beam-background gas interactions over the length of the electrostatic transport section (2.2 m) is expected to be approximately 0.025% (e.g., $I_{B\ \text{loss}} = 0.04$ mA for $I_B = 175$ mA), dominated by stripping ($K^+ \rightarrow K^{2+}$, $\sigma_{K^+ \rightarrow K^{2+}} = 3.5 \times 10^{-16}$ cm^2 [28]), assuming that the background gas mostly consists of N_2 and/or O_2.

E. Numerical simulations

Envelope codes are useful during the design process to determine the main lattice parameters and for controlling and tuning the beam during operation. The coupled envelope equations

$$a'' + ka - \frac{2K}{(a+b)} - \frac{\varepsilon_x^2}{a^3} = 0, \tag{3a}$$

$$b'' - kb - \frac{2K}{(a+b)} - \frac{\varepsilon_y^2}{b^3} = 0 \tag{3b}$$

are numerically integrated, where

$$\varepsilon_{x,y} = 4\varepsilon_{x,y\ \text{RMS}} \tag{4}$$

is the unnormalized ''edge emittance'' of the beam in the horizontal and vertical directions, respectively, and $\varepsilon_{x,y\ \text{RMS}}$ are defined in the appendix [Eq. (A2)]. In Eqs. (3a) and (3b) K is the generalized perveance defined in Eq. (1) and k is the strength of the applied focusing fields. The main difference between the various envelope codes is how the applied fields are described. The simplest description of these fields is the hard-edge equivalent model of the quadrupoles. The focusing fields are then given by

$$k = \frac{V_q}{E_B} \frac{1}{r_{\text{bore}}^2},$$

where V_q is the quadrupole unipolar voltage and is applied over the effective length of the quadrupole. A more realistic model employs the quadrupole component of the multipole decomposition of the 3D field based on the quadrupole geometry and the effect of the E_z component of the applied fields on the envelope and corresponding radial focusing force arising from the varying kinetic energy.

However, the envelope model only describes the statistical edge evolution of the beam and does not include higher order components of the focusing fields or the effect of the image forces that become more important when the beam gets close to the walls. Moreover, other effects like the behavior of halo particles (i.e., particles whose trajectories reside outside the core of the beam) or collective effects such as space-charge waves and nonlinear self-fields are not addressed in an envelope description of the beam and may alter its dynamics. In order to consider the high-intensity beams needed for heavy-ion inertial fusion, we need to take all these effects into consideration. The dynamics of the beam can be studied by calculating the trajectories of many macroparticles, each representing a large number of actual beam particles. Particle-in-cell (PIC) codes such as WARP [29,30], quickly described below, follow this principle.

The WARP code uses plasma simulation techniques to model self-consistently the behavior of high-space-charge particle beams. It allows flexible and detailed multidimen-

sional modeling of high current beams in a wide range of systems, and is being designed and optimized for heavy-ion fusion accelerator physics studies. The core model is the PIC algorithm, which is combined with a description of the accelerator lattice. At present it incorporates a 3D field description, an axisymmetric (r, z) description, and a transverse slice (x, y) description, and includes a simple transverse envelope model for comparison to the RMS moments of the particle distribution. Image forces assume perfect conductors and are calculated at each time step using the capacitive matrix technique [31–33]. Typically, several hundred thousand macroparticles and transverse grid sizes of the order of a few tenths of a millimeter are used in the calculations. At the end of a run, files that contain all the information needed for analysis or to continue the simulation at a later time are generated. Initial particle distributions are typically either Kapchinsky-Vladimirsky (K-V) or semi-Gaussian, but particle distributions constrained by experimental measurements are also loaded into the Python [34] interpreter.

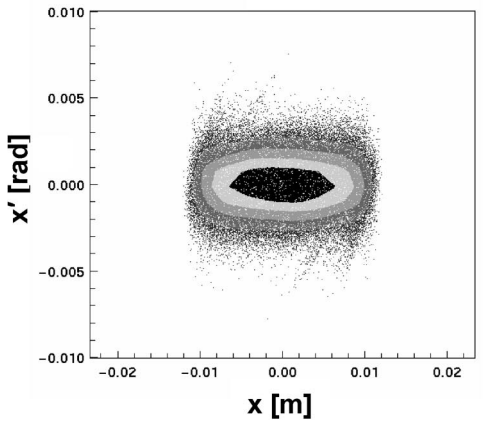

(a)

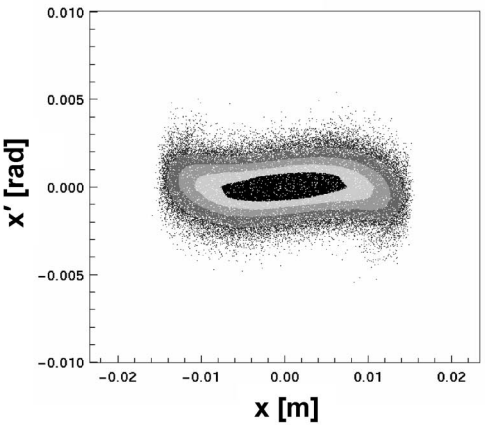

(b)

FIG. 8. Horizontal phase-space plots (simulations) in the HCX tank at the maximum beam excursion, where the beam fills (a) 60% and (b) 80% of the clear bore aperture. The physical aperture is at ±23 mm.

In Fig. 8 we show the phase-space particle distribution obtained from two WARP calculations done for the transport through the HCX electrostatic transport section.

These plots illustrate some of the particle-in-cell simulations that were made prior to building the beam line and which studied the dynamic aperture [35] from a simulation standpoint. These simulations are necessary to set the primary experimental agenda as they indicate which effect might be observable in the experiment and they continue to be used for data analysis. Meanwhile, the results from the experiment are used to improve the reliability of such calculations, which remain idealized in many respects. Effects such as gas desorption due to halo and gas interactions are so far not included in the simulations.

F. Normal operation conditions

The injector has operated at ≥ 2 MV. However, most measurements reported here were made at a beam energy, E_B, of 1.0 MeV. Future measurements will be carried out at higher injection energy (i.e., 1.5 to 1.8 MeV). At $E_B = 1.0$ MeV, the beam current, I_B, is 183 mA (average of the flattop at the exit of the injector) and the number of ions per pulse $N = 6 \times 10^{12}$. Quadrupole voltages in the electrostatic transport section are ± 24.4 and ± 17.5 kV, which correspond to 60% and 80% fill factor for matched and centered beams. Note that the actual beam-edge excursion ($2 \times$ RMS) in the experiment is always slightly larger than 60% or 80% because of residual mismatch and misalignment. The nominal beam and lattice parameters for the data presented in this paper are summarized in Table I.

III. INJECTOR CHARACTERIZATION

The injector has produced up to 0.8 A of K^+ ion beam at 2.0 MV by using a 17-cm diameter contact-ionization source [36]. However, in early work, the beam current density distribution was hollow, inducing nonlinear self-fields. When injected into a linear transport channel, such distributions are far from an equilibrium condition (i.e., where particles are in local force balance) and consequently generate a broad spectrum of collective, space-charge-driven oscillations that can lead to emittance growth during the relaxation process and render the interpretation of the downstream transport experiments more difficult [37–40]. The pulse length was extended for HCX from 2 to 4 μs to allow exploration of the effects due to the buildup of gas, secondary ions, and electrons [21,22]. The optics modifications that included the installation of a smaller source (diameter, $2R = 100$ mm), a new copper Pierce electrode [41], and the reduction of the gate electrode aperture (from 179.5 to 110 mm) produced a more uniform beam suitable for downstream experiments.

During the checks of the injector optics modifications, beam current up to 380 mA at a beam energy of 1.5 MeV

TABLE I. Main beam and lattice parameters in the electrostatic transport section.

	60% fill factor	80% fill factor
Ion energy (MeV)	1.0	1.0
Pulse duration (μs)	4.5	4.5
Ion speed/light speed (β)	0.007	0.007
Pulse length (m)	10.0	10.0
Beam current (A)	0.18	0.18
Brightness (A/mm^2)	0.7	0.7
Quadrupole bore radius (mm)	23.3	23.3
Averaged beam radius (2 RMS) (mm)	10.3	14.7
Field gradient (kV/cm^2)	9.0	6.4
Undepressed phase advance (σ_0) ($^\circ$)	69	48
Tune depression (σ/σ_0)	0.19	0.16
Quadrupole longitudinal occupancy (%)	71	71
Lattice period (cm)	43.3	43.3
Number of quadrupoles	10	10
Electrostatic transport section length (m)	2.2	2.2

and $I_B \approx 600$ mA at $E_B = 1.8$ MeV were measured. Earlier reports [22] indicated that as much as 20% more beam current was predicted by first-principles calculations with WARP than was measured in those experiments. Since I_B is sensitive to the applied extraction voltage, the calibration procedure for the pulse applied to the gate electrode was improved using a procedure described in Ref. [42]. The effective extraction voltage uncertainty from this procedure is $\pm 5\%$, or 0.2% of the beam energy. With the gate electrode voltage thus calibrated, the experimental current falls within 10% of the expected value based on 3D WARP PIC simulations. For future experiments at 1.8 MeV, to maintain similar beam dynamics (i.e., same ion trajectories) as our 1 MeV measurements, we expect to extract 442 mA (scaled from $I_B = 183$ mA at $E_B = 1$ MeV). At higher extraction voltages and $E_B = 1.8$ MeV, the injector delivers at least 600 mA without scraping in the ESQ section.

The Kapton image of the beam after the final optimization reveals a more uniform beam current distribution than earlier measurements (Fig. 9). The 1.5–1.8$\times$ increase in current density previously observed near the horizontal beam edge is absent, and the $\approx 3\times$ density increase previously observed in the vertical beam edge has been reduced to $1.6\times$. Additionally, the overall size of the beam is more suitable for further manipulation downstream in the matching section.

Since the Kapton film image is time integrated, additional time-resolved measurements such as the single-slit current density profiles of Fig. 10 are needed to identify the time dependence of the features in the Kapton image. Stepping through time slices of the transverse current density profiles shows that the structures in the center of the beam (Fig. 9) occur only at the head (i.e., beginning) and the tail (i.e., end) of the beam pulse. For instance, the profile shown in Fig. 10(a) (before diode optimization), where the signal has been integrated over a short flattop portion 3.2 μs after the leading edge of the beam current pulse ($\equiv \tau_0$), indicates that the current density of the beam remains nearly constant except at the edges. As in Fig. 10(a), the profile in Fig. 10(b) (after optimization) also shows a very uniform core, but a much smaller enhancement at the edges. Because of having different current and energy from the main part of the pulse, the head and tail of the beam have very different dynamics than the middle of the beam pulse.

Figure 11 shows the phase-space measurement of the beam in the horizontal and vertical directions after optimization. In these and subsequent phase-space plots (i.e., ''sheared'' phase space), the envelope divergence or convergence of the beam (a' and $b' \sim \pm 40$ mrad) has been removed by the transformation

$$x'_{\mathrm{sh}} = x' - \left[(x - \langle x \rangle) \frac{a'}{a} \right], \tag{5}$$

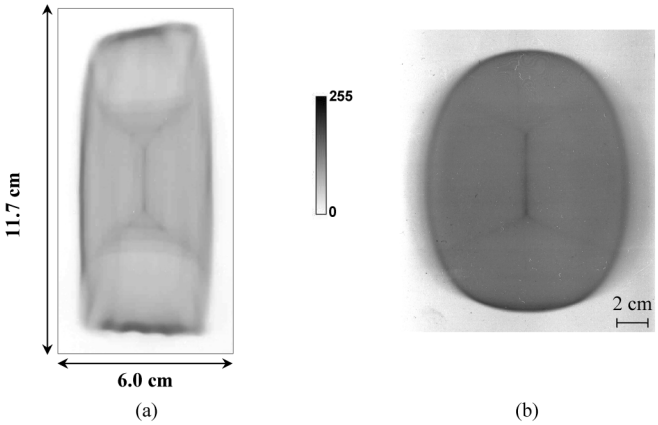

FIG. 9. Kapton film images of the beam at the exit of the injector taken (a) before diode optimization and (b) after diode optimization.

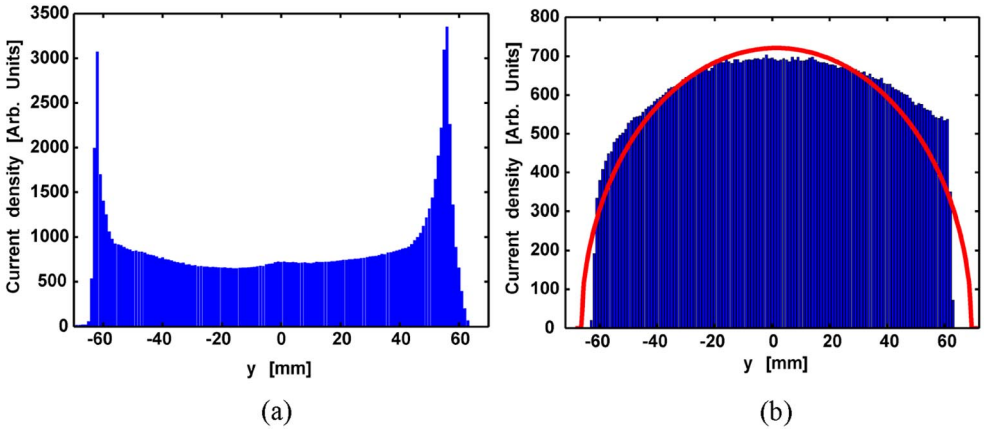

FIG. 10. (Color) Vertical single-slit current density profiles taken at the exit of the injector (a) before final optimization of the diode [summed over $\Delta t = 0.96$ μs, 3.2 μs after the leading edge of the beam current pulse (τ_0)], (b) after final optimization of the diode (summed over $\Delta t = 0.96$ μs, 3.12 μs after start). The summation of the data is done over a short portion of the flattop of the beam current pulse. The red parabola is the equivalent profile for a uniform density beam with the same RMS beam size as the data. The step size is 1 mm for both measurements. Single-slit profiles are measured 22.6 cm downstream of the Kapton film location.

and similarly in the vertical (y) direction. This manipulation is local area preserving so that phase-space distortions (few mrad) are clearly expressed. The red ellipse indicates the area of an RMS equivalent beam with the same emittance. Some of the small scale features in the phase-space plots are artifacts of the sampling step sizes and contouring algorithm.

The normalized emittance listed in Fig. 11 is $\varepsilon_n = 4\beta\varepsilon_{\mathrm{RMS}}$, where $\varepsilon_{\mathrm{RMS}}$ is defined in Eq. (A2). The injector diode retrofits decreased ε_n from 1.7 to 0.9π mm mrad in the vertical direction and from 2.1 to 0.5π mm mrad in the horizontal direction. The theoretical minimum emittance based on the emitter size (radius $= R$) and temperature ($T \approx 1100\,^{\circ}\mathrm{C}$) is

$$\varepsilon_n = 2R\sqrt{\frac{kT}{m}} = 0.18\pi \text{ mm mrad}.$$

Note that in Fig. 11 the ordinate ranges are the same for both plots, though the centers are shifted.

The injector beam characterization measurements and the first measurements through the HCX were made using a contact-ionization source. We switched to an improved alumino-silicate source [43], to avoid the rapid depletion associated with doped contact-ionization sources.

IV. MATCHING SECTION

The matching section compresses the beam area transversely by a factor of ≈ 25 and produces the matched beam envelope parameters a, a', b, and b' necessary for transport in the periodic electrostatic lattice. In this significant beam manipulation, the maximum envelope excursions occur in the first and second quadrupoles, filling up to 80% of the clear aperture there. Figure 12 is an example of the result

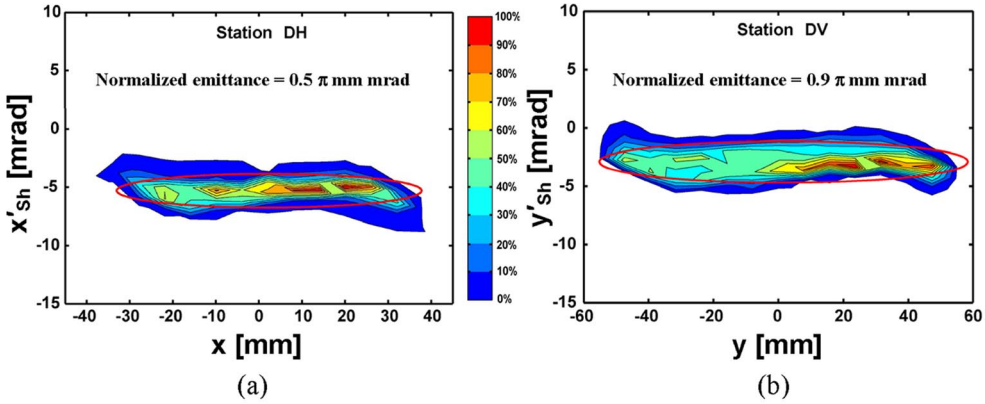

FIG. 11. (Color) Emittance diagrams (sheared) taken at the exit of the injector system after optimization of the injector diode. (a) x-x' (horizontal direction), (b) y-y' (vertical direction). Data shown here have been summed over eight time slices ($\Delta t = 0.96$ μs) corresponding to the flattest part of the beam pulse (3.12 μs after τ_0). The sampling step sizes are 6.2 mm and 0.9 mrad for the horizontal scan and 7.6 mm and 1.1 mrad for the vertical scan.

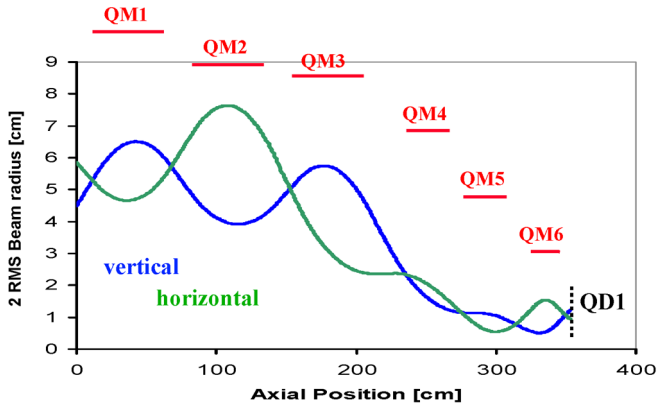

FIG. 12. (Color) Representative envelope calculation of the beam going through the matching section (for the 60% fill factor case in the downstream lattice). The red lines represent the quadrupoles' bore radii.

from an envelope calculation using hard-edge quadrupoles to model the focusing fields.

Typically, the beam centroid exiting the injector is offset from the beam line axis by 1–2 mm and 3–5 mrad. The centroid undergoes betatron oscillations through the quadrupoles of the matching section. The centroid at QD1 is centered by mechanical translation of the three steering quadrupoles QM4–6 in the matching section. The required displacements are determined by calculating the single-particle motion through these quadrupoles, and then solving for the quadrupole displacements needed to center the beam. By this procedure, the beam centroid positions $(\langle x\rangle, \langle y\rangle)$ and angles $(\langle x'\rangle, \langle y'\rangle)$ are centered to within 0.5 mm and 2 mrad, respectively.

Even though the beam fills a relatively large fraction of the aperture (up to 80%) in the early part of the matching section, pickup signals capacitively connected to the quadrupole electrodes indicate that beam loss is minimal through the middle, or flattop, of the beam pulse. This is illustrated in Fig. 13 where the capacitive monitor waveforms for QM1 [Fig. 13(a)] and QM6 [Fig. 13(b)] positive electrodes are plotted. The positive and negative peaks at the head and the tail of the pulse, respectively, are characteristic of the rising and falling image charges of the beam induced onto the quadrupole electrodes when it enters and exits the quadrupole. As a check of the interpretation of the electrode monitor signals, we derived the expected capacitive waveform based on the upstream total beam current diagnostic using Eq. (2) and added it to Fig. 13. The good agreement with the electrode monitors for the head of the beam (see Fig. 13) shows that the monitor signals in the matching section are from the capacitive pickup of the passage of the beam through the quadrupole, except for the very end of the beam pulse, which will be discussed below.

In Fig. 13 the collected signal in the flattop region of the pulse (between the peaks) is very small. Following the discussion from Sec. II D, based on the sum of all six matching section quadrupole pickup signals, we conclude that the beam loss is $<0.5\%$ of the total beam current. Because of the slow fall time of the beam pulse, the tail is mismatched and the beam loss is greater there, as indicated by the large negative spike on the QM6 capacitive monitor waveform (Fig. 13). The strong negative peaks at the tail are attributed to the beam striking the quadrupoles.

The desired envelope parameters at the exit of the matching section were achieved by constraining the envelope model [Eqs. (3)] by QD1 measurements and adjusting the gradients of QM3–6. However, this model does not include effects such as fringe fields, the E_z component of the focusing fields, image forces, and the evolution of the

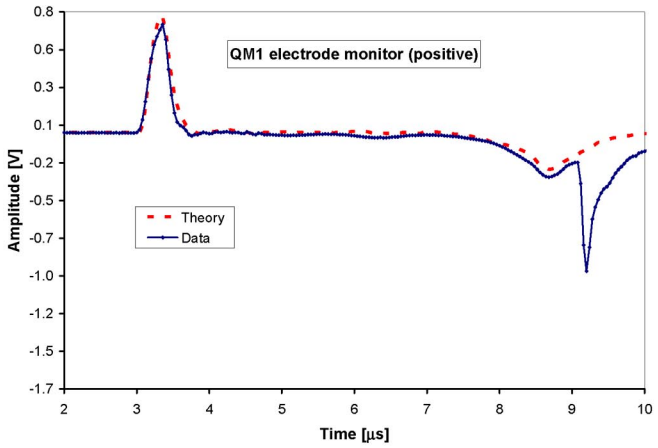

(a)

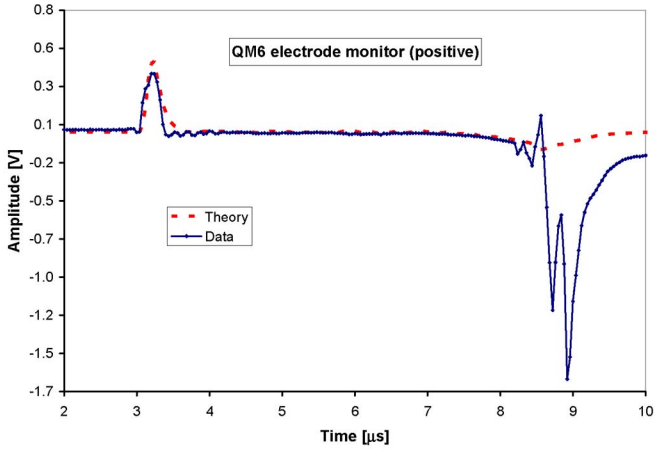

(b)

FIG. 13. (Color) Electrode monitors for the first (a) and last (b) electrostatic quadrupoles of the matching section. The blue curve is the raw signal across 10 Ω. The dashed red curve is the expected signal derived from a current transformer waveform at the injector exit using Eq. (2). Note that the difference in peak amplitude for the head of the beam in the signals collected in QM1 and QM6 is due to the fact that QM6 is 30% shorter than QM1 and therefore the total charge subtended by the electrodes is proportionally lower in QM6.

emittance. Thus, reaching a reasonable agreement between the measured envelope parameters and the targeted ones requires several iterations. In order to reduce the number of iterations and have a better theoretical understanding of the beam dynamics in the matching section, an improved model of the matching section that includes the effects mentioned above is being developed. Nevertheless, after 3–4 iterations, the matching procedure just described determines the required quadrupole voltages such that the envelope parameters at the exit of the matching section are routinely to within 0.4 mm and 2.1 mrad (1σ) of the ideal matched parameters.

The horizontal phase space of the beam measured at QD1 (sheared) is shown in Fig. 14 (top row) for the two fill factor measurements made so far (60% and 80%). From the variance among more than ten independent data sets at the diagnostics stations at the entrance and exit of the transport section and slightly different lattice gradients (i.e., various quadrupole voltage solutions in the matching and transport sections that resulted in the beam filling 60% or 80% of the clear aperture), the estimated emittance measurement uncertainty is 10% (1σ). Though the phase-space distribution is slightly more distorted for the 60% fill factor case than for the 80% fill factor case (based on second and third order coefficients of a third order polynomial fit of $\langle x'(x)\rangle$), the normalized emittance is nearly independent of the matching solution within the experimental uncertainties. However, the beam emittance measured at the exit of the matching section appears to be lower than the one measured at the exit of the injector (by 2.0–2.4 times in the vertical plane and 1.0–1.2 times in the horizontal plane for the 60% and 80% fill factor cases, respectively, Fig. 11). Since a subpercent beam loss cannot account for such a large discrepancy, these differences point to a large overestimation of the emittance measurements made at the exit of the injector due to systematic instrumental errors. There are three effects: the finite width of the slits, the misalignment of the slits with respect to one another (i.e., slit and slit-cup not exactly parallel to one another), and the rotation of the beam principal axis with respect to the main axis of the transport channel (horizontal and vertical, on which the slits are aligned). The errors due to finite slit width account for $\leq 1\%$ increase in the perceived emittance for all measurements. Both alignment effects increase the apparent beam emittance, and are pronounced when the beam is large ($a \approx 40$ mm and $b \approx 60$ mm as at the injector exit) and are negligible when the beam has been transversely compressed by the matching section

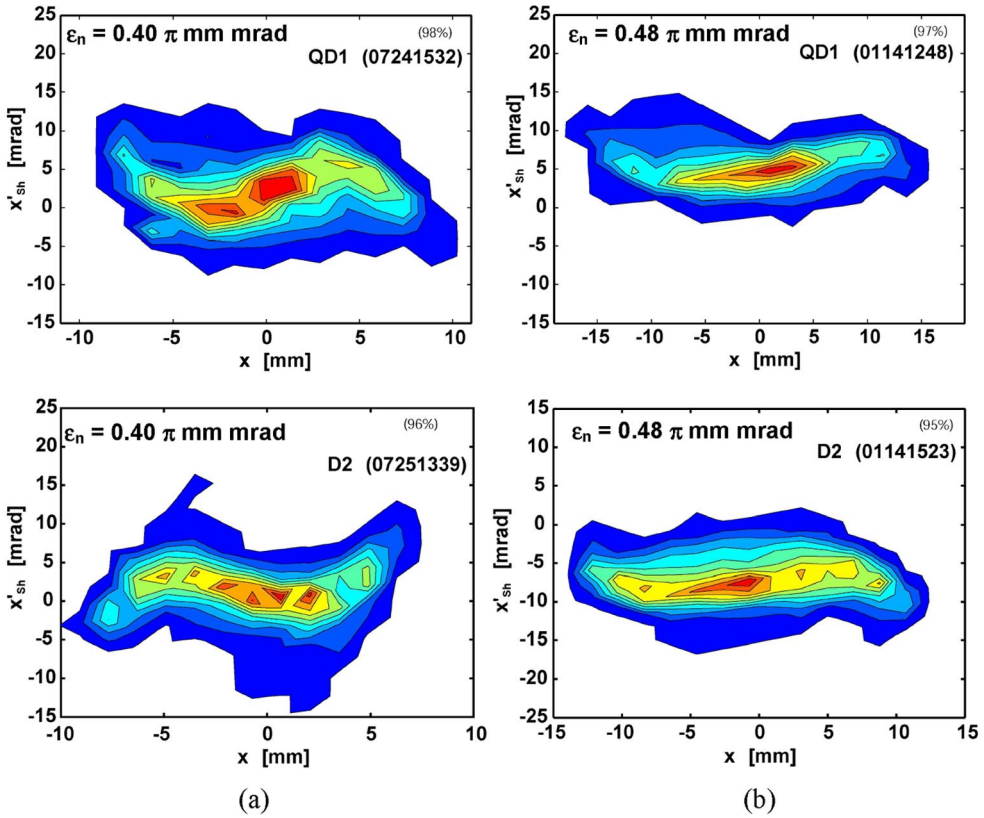

FIG. 14. (Color) Horizontal phase-space diagrams before (top) and after (bottom) the electrostatic transport section for (a) 60% fill factor and (b) 80% fill factor, for time slice t_A (in Fig. 16). For the 60% fill factor, the sampling step sizes are 1.5 mm and 2.3 mrad at QD1 and 1.4 mm and 2.2 mrad at D2. For the 80% fill factor, the sampling intervals are 2.1 mm and 1.9 mrad at QD1 and 1.9 mm and 1.8 mrad at D2.

($a \approx 10$ mm, $b \approx 15$ mm). A Monte Carlo simulation of particles followed through the emittance scanner shows that the larger emittance at the injector exit may be explained by a transverse beam rotational misalignment of $\approx 1.5°$ plus the slit and slit-cup misaligned by 0.25 mrad. Additionally, 3D PIC simulations of the HCX experiment indicate that the emittance should (initialized with a semi-Gaussian distribution at the matching section entrance) remain constant in the matching process or increase by 1.3 times (simulations started at the ion emitter surface) [44].

Furthermore, the measured emittance depends on the sampling step size of the measurements. Increasing or decreasing the step size by a factor of 2 contributes to a $\approx 2\%$ difference in the calculation of the emittance, based on linear interpolations of the data.

The uncertainties for the beam envelope parameters were characterized by calculating the standard deviation (1σ) of five repeated measurements, where the data were summed over a 1.5 μs window near the flattop region of the beam current pulse. By this measure, the stability and reproducibility of the envelope coordinate (a, b) and angle (a', b') measurements are ≈ 0.3 mm and $1 \approx$ mrad, respectively, which includes the effect of the beam current drift over the course of the measurement (~ 1 h) of up to ≈ 2 mA out of a nominal beam current of 183 mA.

V. BEAM CURRENT TIME DEPENDENCE STUDY

The head and the tail of the beam pulse, where the current rises or falls through 0–95% of the maximum, have very large systematic variation in envelope parameters, inevitably leading to envelope mismatches. But, partly because of the lower beam current, we find that for the head the envelope can remain confined with negligible beam loss. However, even in midpulse, as much as 50% variations in beam size and angle were observed at QD1 (for a 60% fill factor solution) when the beam current varied by $\sim$15% in early measurements (Fig. 16). The time dependence of the envelope parameters emerging from the matching section is driven by variations in the extraction voltage which controls most of the emission (and therefore the beam current) at the beginning of the injector. The downstream trajectories in the injector differ greatly with current when the extraction voltage varies independently of the Marx voltage. This is in contrast to the situation where all the injector voltages are scaled together and the trajectories are identical. Such sensitivities were predicted by 3D PIC simulations of the injector followed with envelope simulations through the matching section.

The strong correlation between beam current and envelope parameters is illustrated in Figs. 15 and 16, which show measured current waveforms and the corresponding measured envelope parameters, b and b', before and after extraction voltage waveform tuning, for which the time

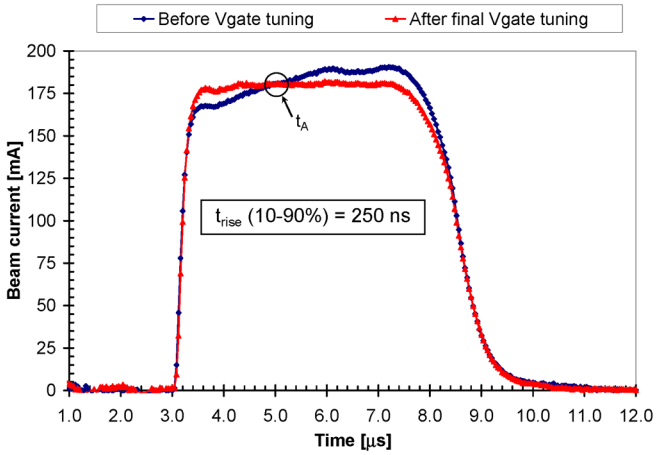

FIG. 15. (Color) Beam current comparison [before (blue) and after (red) extraction voltage adjustments] measured at the exit of the injector with a current transformer.

dependence is significantly different. A time slice t_A at which the beam current waveforms at the different times intersect (Fig. 15) is identified. The corresponding time slice at QD1 (Fig. 16) is also identified. Note that the measured envelope parameters at this time slice intersect to within the measurement uncertainties.

The beam current pulse was flattened by tuning the gate voltage pulse. After the corrections, the beam current is flat to within 1.5% over a 3.1 μs window in midpulse (Fig. 15). As a result, the beam envelope parameters vary by less than 15% over that same time window. The sensitivity of the envelope radii and angles to beam current (as well as energy) is important in determining the maximum fill factor since variations in these parameters drive the beam envelope evolution along the pulse length. For instance, if for a given time slice the beam parameters are such that it would undergo large envelope mismatch oscil-

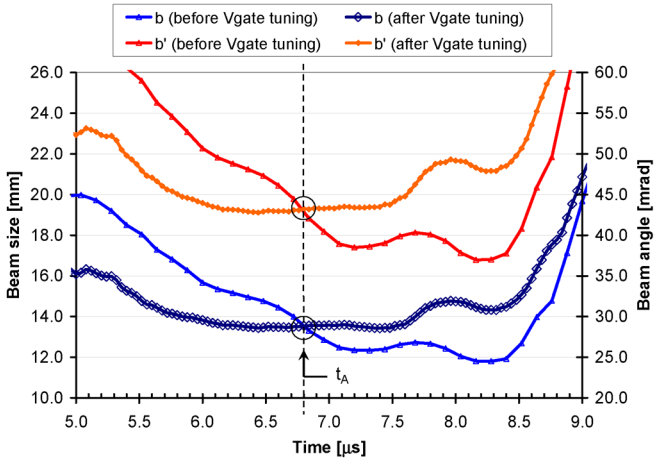

FIG. 16. (Color) Vertical envelope parameters [b (dark blue and light blue curves) and b' (red and orange curves)] at QD1 diagnostics station as a function of time before and after the extractor voltage adjustments.

lations leading to beam scraping somewhere in the lattice, the transport of the rest of the beam pulse would be affected or even prevented.

VI. TRANSPORT THROUGH ELECTROSTATIC QUADRUPOLES

Ideally, the fill factor experiment would be done using constant current density beams of various sizes, for which $I_B \propto a^2$ and the interior trajectories are self-similar. We chose to vary the tune and matching to achieve various fill factors, but at varying current densities. Alternative techniques such as the use of apertures and making several ion sources of different sizes were deemed too complicated or too expensive. In particular, the beam aperturing process can induce significant undesirable complications (e.g., desorbed gas and secondary electrons production) that may distort the beam in the transport section. PIC simulations of the experiment in which various fill factors were achieved either at fixed current density or by varying the quadrupole tune gave similar results [45], giving confidence that the experimental approach (i.e., exploring the fill factor by decreasing the lattice focusing strength) will give information relevant to the driver case.

We have made two fill factor measurements, for the envelope filling 60% and 80% of the available bore diameter in the transport channel of ten electrostatic quadrupoles arranged in a periodic lattice. For each fill factor measurement, the transverse phase space of the beam was characterized in detail at the exit of the matching section, as discussed in Sec. IV. Each case required a different matching solution (i.e., different quadrupole voltages in the matching section). Because the fill factor was changed by tuning the upstream beam to the matched beam conditions in the transport section for a lower focusing gradient, rather than by changing the current, the undepressed betatron phase advances per lattice period (σ_0) for the two fill factors are different (69° and 48° for the 60% and 80% fill factor cases, respectively). The depressed phase advances per lattice period (σ) due to the self-potential of the beam are 13° and 8° for the 60% and 80% fill factor cases, respectively.

Similar to the matching section results, in the entire length of the electrostatic transport section, considering the midpulse and both fill factor cases, beam loss is 1%. This is based on the sum of the currents collected on all ten quadrupole electrodes interpreted per Sec. II D, which indicate particle loss of $<1\%$ and the ratio of Faraday cup currents at the entrance and exit of the transport section indicating 1% loss. The quadrupole electrode pickup signals used for determining the sum of the collected currents in the middle of the pulse for 80% fill factor measurements are shown in Fig. 17. The pickup signals at the head and tail of the beam are the result of a combination of both the capacitive response and the collected currents and are difficult to interpret. Moreover, because of the intrinsic

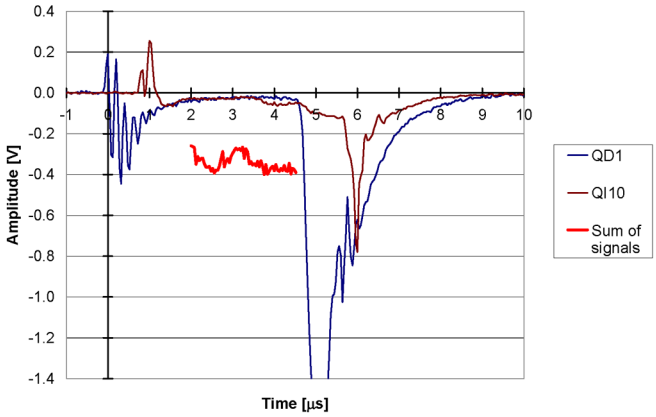

FIG. 17. (Color) Electrode monitors for the first (blue) and last (brown) electrostatic quadrupoles of the transport section for an 80% fill factor case. In red is the sum of all ten quadrupole pickup signals in the middle of the beam pulse. This sum is representative of the beam loss through scraping and beam/background gas interactions.

mismatch of the head and tail of the beam, the individual electrode monitor signal amplitude is smaller or in some instances negative at the beginning of the pulse and is more negative at the end of the pulse, indicating more beam loss at the extremities of the pulse.

From Fig. 14, it can be seen that within the experimental sensitivity there is no evidence of emittance growth at the end of the electrostatic lattice for both the 60% and 80% fill factors in the horizontal plane. This result is also true for the vertical direction (diverging plane). Note also that the details of the beam phase-space distribution remain practically unchanged except for the small ''hooking'' regions that mirror one another between QD1 and D2. PIC simulations initialized with semi-Gaussian distributions [35,45] have also predicted that matched beam excursions filling 80% of the quadrupole bore would result in negligible emittance growth, assuming perfect alignment and envelope control. However, these simulations do not include nonideal effects resulting from particle losses. To date, comparisons of measured phase-space distributions to PIC simulations show that the measured distributions are not well reproduced in the theoretical model, even when initialized with a distribution reconstructed from the data (see Sec. VII). Note that in Fig. 14 the signal-to-noise ratio for the QD1 data sets is $\approx 5\times$ larger than for the D2 data sets.

Integrating the envelope equation from QD1 to D2 (initialized with QD1 measurements of envelope radii, convergence angles, current, and measurements of beam energy) gives a calculated envelope in agreement with the experiment at the D2 location to within 0.4 mm and 3 mrad. This level of agreement allows us to confidently rely on envelope model predictions (such as Fig. 18) to tune the lattice and control the beam envelope excursions in the experiment. Early calculations of the envelope showed discrepancies as large as 25%. After including the follow-

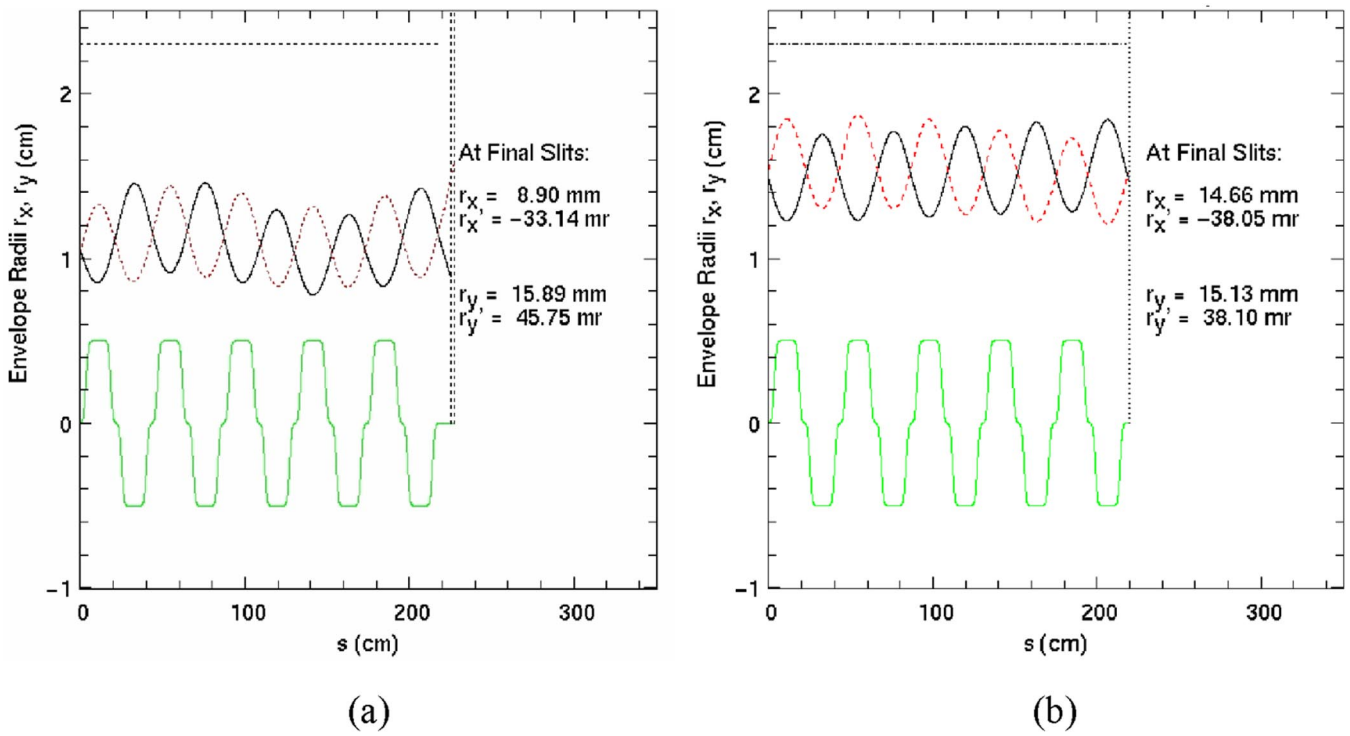

FIG. 18. (Color) Calculated envelope from QD1 to D2 for (a) a 60% fill factor case and (b) an 80% fill factor case. Runs are initialized with data taken at QD1. Black: horizontal direction; red: vertical direction; green: focusing forces quadrupole gradients.

ing effects in the theoretical model, as well as a more accurate determination of the beam current, the beam energy and the variation of the beam parameters over the pulse, the agreement was good as indicated above. The improvements to the model were (1) realistic quadrupole fringe fields based on 3D field calculations, (2) quadrupole E_z from the 3D lattice structure and corresponding radial focusing force, and (3) corrections due to the grounded slit plates of the intercepting diagnostics that short out the self-field of the beam near the diagnostic [46]. In Fig. 18, examples of calculated beam envelopes with these improvements are plotted. In Table II, envelope measurements at the exit of the electrostatic lattice for two 80% fill factor data sets are compared to predictions of the envelope model. Envelope simulation uncertainties are taken from the standard deviation of a Monte Carlo distribution of envelope predictions through the transport section, where several thousand envelopes are calculated with initial conditions randomly distributed about the measured values. The initial distributions for the parameters that are varied are Gaussian with standard deviations representing the measurements' uncertainty and the equipment accuracy (e.g., stability of the quadrupole voltages) previously discussed.

The uncertainties for the data at D2 are estimated as for the QD1 uncertainties described in Sec. IV. Thus, the RMS envelope model is accurate to within the measurement uncertainty.

TABLE II. Experimental envelope parameters compared to envelope model predictions at the exit of the electrostatic section for two 80% fill factor cases. Note that in this table, data sets A and B were taken at different z locations in the lattice, as pointed out in Sec. II D. The data are from a 120 ns interval of the flattop region of the beam pulse, 2.64 μs after τ_0.

		a (mm)	a' (mrad)	b (mm)	b' (mrad)
Data set A	Experiment	12.24	−38.52	21.10	43.04
	Env. model	12.07	−35.46	20.95	46.10
Data set B	Experiment	14.07	−38.50	15.54	39.84
	Env. model	14.66	−38.05	15.13	38.10
Uncertainty ($\pm 1\sigma$)	Experiment	0.3	1.0	0.3	1.0
	Env. model	0.5	2.1	1.2	3.0

Further data analysis shows that RMS beam parameters are more sensitive to beam current variations for a 60% fill factor case than for an 80% fill factor case.

Defining the envelope mismatch as $\delta_M = \max(a_{\max}, b_{\max}) - R_{0,\max}$, where $\max(a_{\max}, b_{\max})$ is the maximum of the envelope excursions in both planes of the calculated envelope initialized with QD1 measurements, and $R_{0,\max}$ is the maximum excursion for the theoretical matched beam, for both fill factor cases shown in Fig. 18, we were able to match the beam to within $\delta_M = 1 \pm 0.5$ mm. The uncertainty in δ_M is based on the Monte Carlo analysis discussed above.

Envelope simulations for which the quadrupole voltages were allowed to vary randomly by the expected tolerance on voltage control (0.1 kV or $\approx 0.5\%$) about their nominal value, including the experimental constraint that five of the ten quadrupoles are energized with common power supplies, indicate that the average envelope mismatch excursion grows by 0.2–0.3 mm over the first five lattice periods. This rate decreases to less than 0.1 mm per five lattice periods after transport through 50 lattice periods.

With the beam centered to within 0.5 mm and 2 mrad upstream (QD1), we observe 1–2 mm and 1–5 mrad centroid offsets after these ten quadrupoles and the beam centroid varies by ≤ 0.5 mm and ≤ 1 mrad during the flattop of the beam pulse. However, the predicted centroid values from simulations do not agree with the downstream beam measurements. The quadrupoles were aligned with respect to their common support rail to within ± 100 μm. There is no common misalignment of the quadrupole support rail that satisfies all the data sets. Dipole fields from image charges in the ten transport quadrupoles or induced by the image charge of the beam on the support slit scanner paddles in the relatively open diagnostic regions may be responsible for the discrepancy. However, it was observed that upstream (QD1) beam centroid offsets as large as 2 mm and 5 mrad would not lead to any noticeable beam loss or emittance growth in the electrostatic transport section.

VII. BEAM CHARGE DISTRIBUTION

From crossed-slit measurements (i.e., perpendicular slits upstream of a Faraday cup, each sampling the beam distribution in $\Delta x = \Delta y = 1$ mm intervals) at QD1 and D2, the time-resolved current density distribution $J(x, y, t)$ (see Fig. 19) of the beam was measured. Depending on the applied focusing strength in the matching and transport sections, J may be peaked or hollow in radial profile. The initial nonuniformities in the current density distribution arise from the diode spherical aberrations [22]. Also, the shape of the transverse beam profile exhibits diamondlike

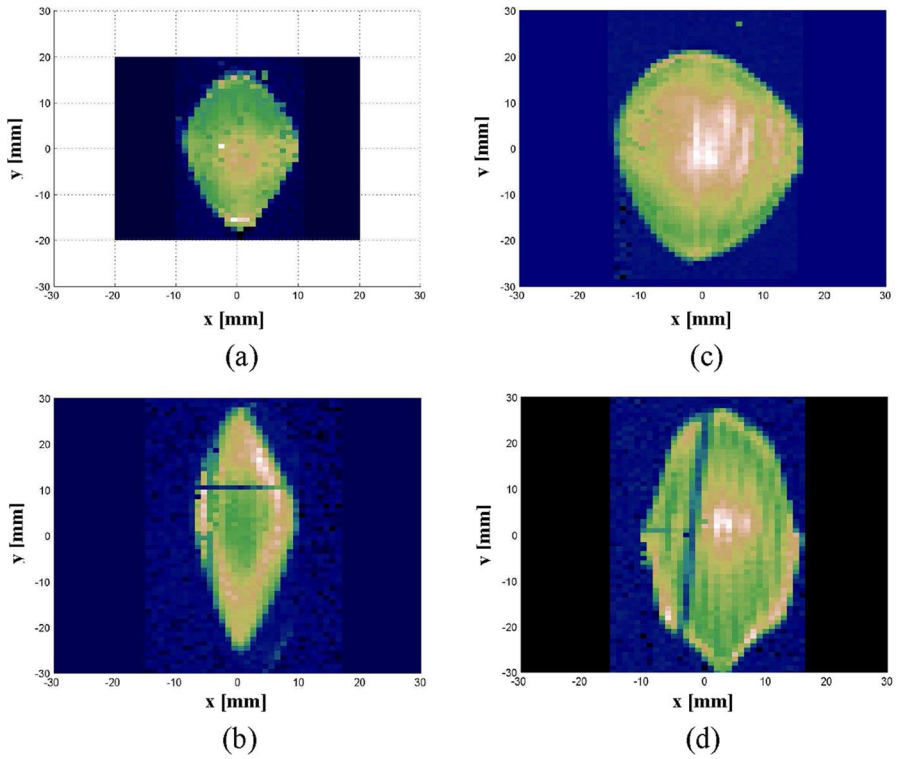

FIG. 19. (Color) Beam current density profiles $J(x, y)$ measured with crossed slits. (a),(b) 60% fill factor case at QD1 and D2, respectively, single time slice ($\Delta t = 0.12$ μs) taken 2.64 μs after τ_0; (c),(d) 80% fill factor case at QD1 and D2, respectively, single time slice ($\Delta t = 0.12$ μs) taken 3.12 μs after τ_0. In (b) and (d) the dark crossed (or line) pattern that is seen comes from bridges across the slits that are there to strengthen the slit structure and avoid deformations.

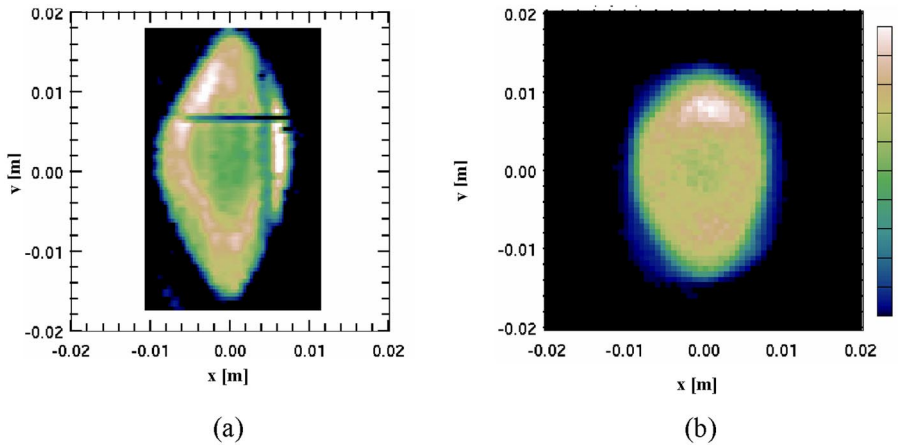

FIG. 20. (Color) Beam current density profiles $J(x, y)$ at midpulse (2.64 μs after τ_0) (a) data at D2, (b) WARP simulation at D2 initialized with data at QD1, projected to a common plane in the lattice. Spatial hollowing in the center of the beam distribution is a common feature to both the data and simulation.

distortions from ideal elliptical symmetry at both diagnostics stations. Transverse oscillation frequencies (e.g., plasma, space-charge wave and envelope oscillations frequencies) are influenced by the change in σ_0 associated with the two fill factor measurements. As a result, different current density distributions were observed.

The diamond-shaped pattern is attributed to nonlinear fields arising from the space-charge component of the distribution and the collective evolution of the distribution in the ESQ injector and in the matching and transport sections. The fact that the 60% fill factor beam, though having smaller radius, is more diamond-shaped than the 80% fill factor beam indicates that nonlinearities from the image forces and the applied fields in the transport section do not play a significant role. Most of the distortion is initiated upstream, in the injector and matching section.

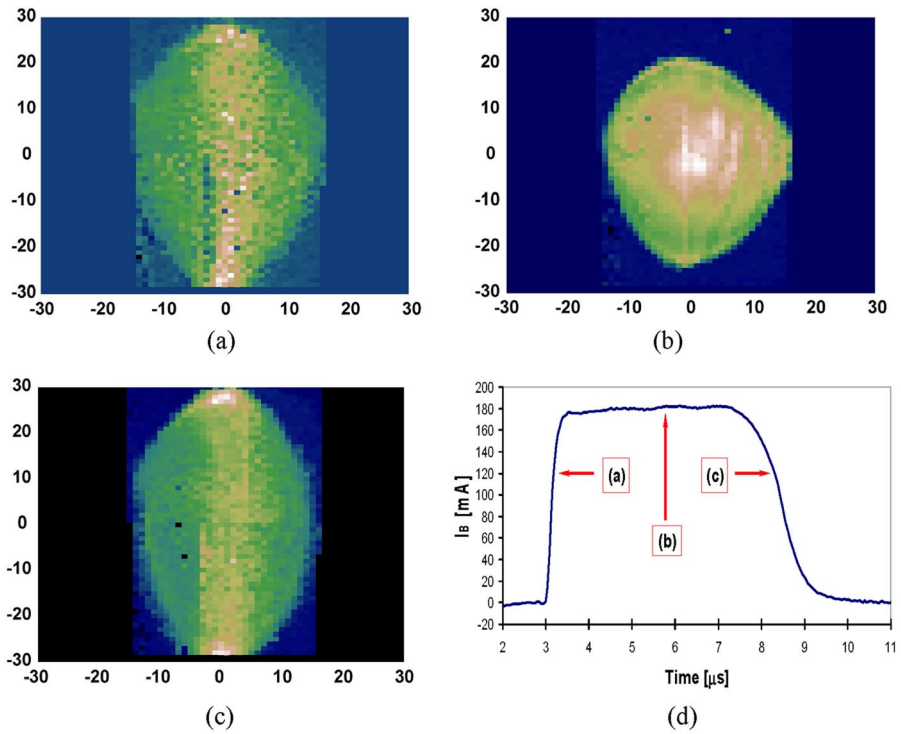

FIG. 21. (Color) Beam current density profiles $J(x, y)$ at QD1 for the 80% fill factor case. (a) Head of the beam (0.36 μs after τ_0); (b) midpulse (3.12 μs after τ_0); (c) tail of the beam (5.04 μs after τ_0; (d) injector beam current waveform showing the total beam current and locations in the pulse for the density profiles in (a)–(c). Time jitter is responsible for the noisier pictures in (a) and (c), which were taken over 4000 pulses.

Simulations [47] indicate that the peaked and hollow patterns are due to transverse space-charge waves that move rapidly in and out of the body of the beam (from Refs. [48,49] $\omega_{\text{space charge wave}} > \omega_{\text{plasma}}$ for all modes). Therefore, the details of the beam current density distribution vary with the longitudinal position in the lattice.

The $J(x, y)$ data are used with the phase-space data at QD1 to construct a consistent particle distribution for simulation studies [44]. Figure 20 shows the first PIC simulations of the beam initialized with a distribution reconstructed from measurements of the 60% fill factor case at QD1. The simulation uses 2×10^5 particles on a 0.2 mm grid and the focusing fields were obtained from a multipole decomposition of the calculated electrostatic field based on the mechanical design of the HCX quadrupoles.

Both the simulated and measured beam configuration space distributions are hollow (center to edge $\approx$ 1:2) but the distributions are different. However, second order parameters such as the RMS beam size and convergence/divergence angles differ significantly between the experiment and the simulation. Several items contribute to the disagreement: First, the reconstruction algorithm (still under development) does not exactly reproduce the initial measured second moments of the beam at QD1. In particular, a' and b' differ from the experiment by 1 mrad. Then, the beam energy for this data set is not known to better than 5% to 10%. Combined, these two sources of error could account for as much as 10 mrad and 2 mm differences in the beam envelope parameters expected at D2. Another effect which is not yet taken into account in PIC calculations is the beam self-electric field shorting out by the measuring slit [46]. Envelope calculations including this effect show that it contributes to another $\approx$ 0.5 mrad difference to the final beam envelope angles expected at D2. Finally, the measurement of the 4D phase space with the standard slit/slit-cup diagnostics is incomplete, since only the $x - x'$, $y - y'$, and $x - y$ projections are measured. In order to realistically describe the detailed evolution of the beam distribution, the full 4D phase space needs to be known, since cross correlations exist between the vertical and horizontal projections [$f(x, y', t)$, $f(y, x', t)$, and $f(x', y', t)$]. A new optical diagnostic (discussed in Sec. II D) measures the missing projections of the 4D phase-space distribution and will improve our ability to simulate accurately the beam throughout its transport in the electrostatic section and beyond.

The time-resolved crossed-slit data show that at QD1 the profile of the beam during the rise and fall of the beam current pulse and for both fill factors is larger than during the flattop (Fig. 21).

Ballooning of the beam head was predicted for the beam exiting the injector from time-dependent 3D particle-in-cell simulations and is attributed to an extraction voltage rise time in the diode presently too slow to match the space-charge field of the beam head [50,51]. The calculations also suggest that a 50% decrease of the rise time would greatly reduce such ballooning and avoid early scraping in the injector. With modifications to the extraction circuit straightforward to implement, the extraction voltage rise time was decreased by 30%. Preliminary measurements at QD1 and D2 did not show any significant change in the RMS beam parameters in the beam head at the exit of the electrostatic transport section. However, it is possible that the effect of the faster rise time on the beam envelope is obscured by the large compression and mismatch of the head through the matching section, for instance, if the head scrapes early in the lattice. Calculations of the head-tail dynamics through the rest of the HCX are underway.

Halo measurements for the 60% fill factor case using single-slit profiles upstream and downstream of the trans-

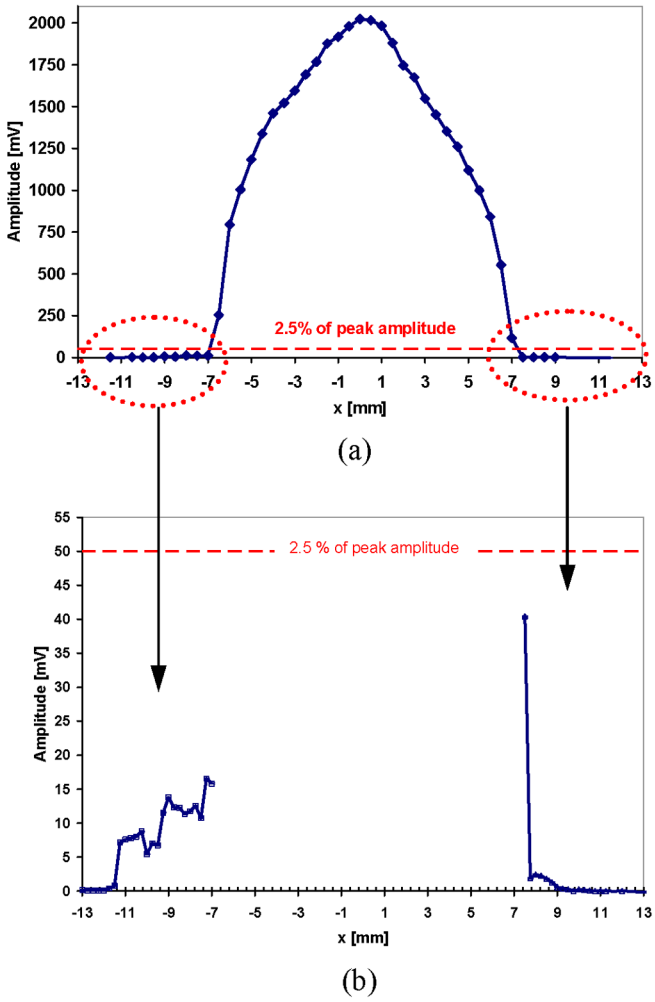

FIG. 22. (Color) Single-slit profile measurements showing the extent of the halo and our present diagnostics' sensitivity for a 60% fill factor case at QD1 (horizontal direction). (a) is a typical whole beam profile; (b) are partial profiles (acquired close to the beam edges only) with 100× greater gain on the oscilloscope. Error bars are smaller than the plot points.

port section and for both directions (x and y) indicate that the beam profile intensity ≈ 5 mm from the steep edge of the beam distribution falls to the order of 10^{-3} of the peak density in the core of the beam, the sensitivity limit with present slit-cup diagnostics. This is illustrated in Fig. 22, which shows single-slit intensity profile measurements of the beam at the exit of the matching section.

VIII. ABSOLUTE BEAM ENERGY MEASUREMENTS

Two new diagnostics, an electrostatic energy analyzer and a time-of-flight pulser (see Sec. II D) were installed to more precisely determine the beam energy and for longitudinal phase-space measurements, though the energy resolution is not small enough to resolve the temperature component.

Figure 23 shows the longitudinal energy distribution obtained with the EA. The 10% higher energy head and long low-energy tail are a combined effect of longitudinal space charge, which accelerates particles at the front end of the pulse and decelerates particles at the rear of the pulse, and the extraction voltage pulse shape. In particular, the slow fall time of the extraction voltage pulse causes the tail energy variation to be twice as great as the variation of the head. These data also show that, in the middle of the pulse, the mean beam energy $\langle E_B \rangle$ is constant to within 0.5% for 3.1 μs.

Figure 24 shows the perturbation produced by the TOF pulser on the beam current waveform, as measured downstream, along with a theoretical calculation of the expected perturbation based on a 1D cold-fluid model [38]. Because of our relatively short beam line, the peaks of the forward- and backward-traveling waves have not yet clearly separated. The energy perturbation is applied by raising the potential of the first matching section quadrupole with respect to its neighbors, which induces a perturbation in the gaps preceding and following the quadrupole, each perturbation resulting in two waves that propagate in opposite directions. These four waves interact with one another while traveling down the beam line, adding some complexity to the observed current waveform perturbation downstream. The beam energy is determined by fitting the model to the data using the beam energy as the only independent parameter.

The TOF and EA diagnostics both determine the absolute beam mean energy to $\pm 2\%$, with both measurement methods agreeing within these uncertainties (Fig. 25). Errors for the EA measurements mostly arise from the calibration procedure (uncertainty of the hole-plate bias voltage and of the fitted K^{2+} ion energy change due to the bias). The dominant source of error for the TOF measurements is determined by the fit between the model and the data. Other errors include the determination of the distance between the z location of the kicker and the measuring plane, the timing of the cables, and the time at which the perturbation is applied.

Before these measurements, the beam mean energy was estimated to be 1045 keV, based on the calibration of the capacitive probe that monitors the Marx voltage near the high voltage dome. This calibration is performed at low voltage and at atmospheric pressure in the dome, in a geometric configuration slightly different from normal operation. From the energy analyzer, the beam mean energy is 962 keV ($\pm$ 2%), almost 10% lower than determined by the capacitive probe. These measurements then provide an independent calibration of the capacitive probe, which monitors the injector voltage on every shot. The precise determination of the energy is essential for the

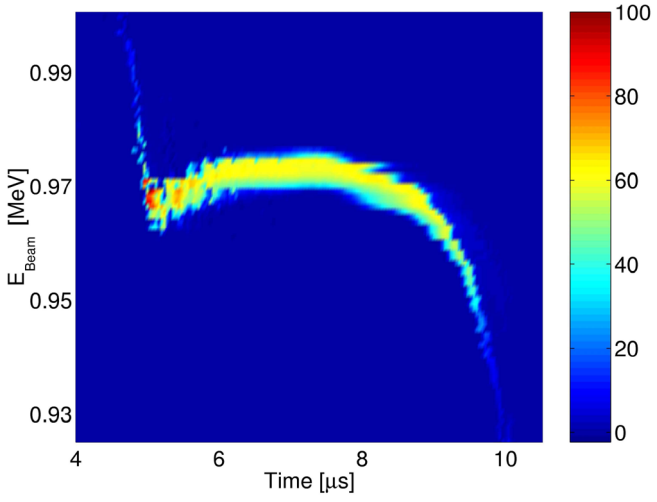

FIG. 23. (Color) Longitudinal energy distribution measured with the electrostatic energy analyzer. K^+ ions were detected at the beam head with 1.1 MeV (not visible on this scale).

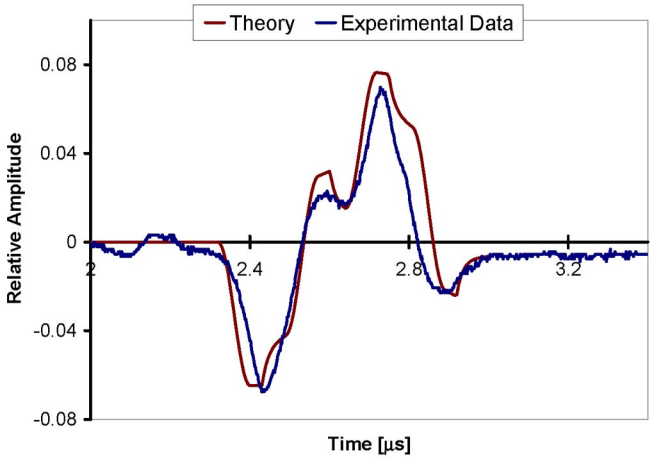

FIG. 24. (Color) Cold-fluid model versus measurement of the perturbation on the beam current waveform. Initial perturbation applied at $t = 0$. The beam energy is the only fitted parameter for the cold-fluid model. The upstream voltage pulse waveform and pulsed quadrupole length was input to the model calculation.

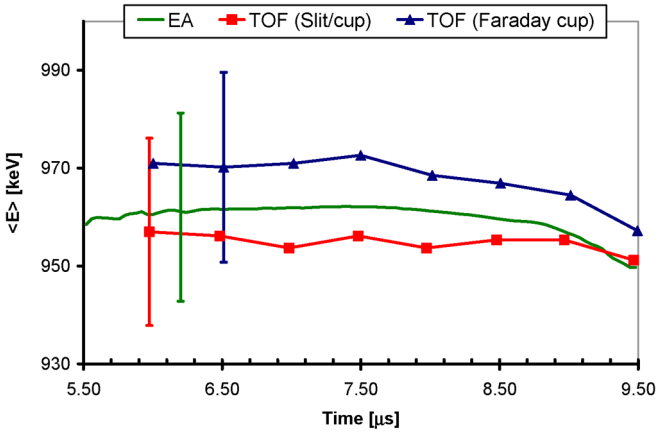

FIG. 25. (Color) Comparison between the time of flight and the energy analyzer measurements of the beam mean energy. In blue and red are the results from the TOF measurements. In green is the result of the energy analyzer measurement.

agreement between envelope simulations and experimental data in Secs. VI and VII. For example, a 2% energy variation at the injector exit induces as much as 20% beam size variation in the vertical direction at the matching section exit.

IX. DISCUSSION

In the electrostatic transport section, the data agree well with envelope calculations that include realistic fringe fields and the effects of the intercepting diagnostics. Additionally, the relative sensitivity to beam current variations shown in the 60% fill factor data versus the 80% fill factor data is understood in terms of envelope mismatch oscillations, which arise when one or more of the terms in the envelope equation is perturbed (i.e., small variations around the ''matched beam'' conditions) [38,52]. In an AG lattice, envelope oscillations can be decomposed into the combination of two fundamental modes equivalent to the breathing and quadrupole modes derived from a continuous focusing analysis, but at slightly different characteristic frequencies [38]. Using an envelope model in which the beam current is varied for otherwise matched parameters, Fourier transforms of the calculated envelope suggest that the current perturbations excite the breathing mode more strongly compared to the quadrupole mode. For the 80% fill factor case, where the undepressed phase advance per lattice period, σ_0, is 48°, the total phase advance of the breathing mode envelope oscillation through ten quadrupoles (i.e., five lattice periods) is $\approx 360°$. Thus, the envelope parameters should show a reduced sensitivity to small beam current variations, in line with the observations. The improved envelope model will improve our ability to manipulate the beam envelope for further experiments, such as launching almost pure envelope mismatch modes (quadrupole or breathing), and to predict the proximity of the 2 RMS beam edge to the bore aperture. The agreement between model and experiment supports the expectation that electrons are promptly swept out of the path of the beam by the focusing electric fields.

Beam steering using 2–3 movable quadrupoles, which requires a good knowledge of the focusing fields and relative displacements of the quadrupoles, is successful at recentering the beam. However, the predictions of the beam centroid trajectory over the length of the transport section, which requires absolute measurements of misalignments of the focusing elements and diagnostics with respect to the system center line, are not as accurate (≈ 3 mm, ≈ 6 mrad) as the predictions of the envelope parameters (< 0.5 mm, ≤ 3 mrad). Image charges and stray dipole due to asymmetric boundary conditions at the diagnostics while acquiring the data may explain this discrepancy. Transport lattices for HIF will have centroid corrections periodically. Understanding the accumulation of centroid errors is important for determining the frequency of correction elements.

The time dependence of beam parameters is also important when defining the limit of the transportable current. The envelope variations throughout the beam pulse inherently lead to a mismatch that can be severe. The time dependence of the beam parameters near the head of the beam pulse shows that the injector waveform rise time is critical for beam matching since this manipulation involves rapid envelope transitions and could easily deteriorate the beam pulse uniformity (as a function of time) at the beginning of the accelerator. Time-dependent focusing gradients to match the beam head might be possible depending on required specifications and cost. At the head of the beam pulse, size and angle mismatch may disrupt the propagation of the rest of the pulse, especially in magnetic focusing transport channels where secondary electrons may be trapped in the rising beam potential. Aperturing the beam in order to scrape off the beam head must be done at a few lattice locations where the envelope excursion of the beam head is relatively large, and may be implemented in future experiments. The ''ballooning'' of the head is minimized when the extraction pulse waveform is tailored such that its rise time matches the space-charge field buildup at the emitter [51].

Also, from halo scrape off at the head and flattop of the beam, gas atoms from the wall are released. The gas atoms will intercept the beam path and induce further loss depending on the atom velocity, the beam edge to wall clearance, and the pulse length.

The velocity tilt for pulse compression at the beginning of a fusion driver in an electrostatic quadrupole transport channel results in a beam whose transverse size increases throughout the pulse (smaller head, bigger tail) while its length remains constant. Although WARP simulations show that during this manipulation the beam remains nearly matched for all time slices, one must take into account these variations in envelope excursion throughout the beam

pulse when assessing the acceptable fill factor, and allow for a range of envelope sizes.

The injected beam is nonuniform in current density as a function of x and y, and remains so for the length of the present beam line as shown by current density measurements at D2 (Sec. VII). The nonuniform distribution induces transverse space-charge waves that oscillate as the beam propagates. The current density distribution differences seen at the exit of the electrostatic transport section between the two fill factor measurements can be explained qualitatively using a warm-fluid description of an intense beam equilibrium [53] and are also consistent with a full kinetic treatment for an AG lattice as calculated by Hofmann *et al.* [49]. Although the theory is developed for small amplitude perturbations in axisymmetric geometry, it appears to have predictive power in our nonideal context. In this context, the normalized frequency $|\frac{\omega}{\nu_0}|$ of axisymmetric flute perturbations as a function of the tune depression $\frac{\nu}{\nu_0}$ for a K-V beam equilibrium in the electrostatic approximation is given by the dispersion relation [53]

$$\left(\frac{\omega}{\nu_0}\right)^2 = 2 + 2\left(\frac{\nu}{\nu_0}\right)^2(2n^2 - 1), \tag{6}$$

where n is the radial mode of the perturbation, whose radial profile can be described by a series expansion of Legendre polynomials of degree n,

$$\nu = \sigma\frac{v_B}{L} \tag{7a}$$

and

$$\nu_0 = \sigma_0\frac{v_B}{L} \tag{7b}$$

the depressed and undepressed betatron frequencies, with ν_B being the ion velocity and L the lattice period. Since for both fill factor cases the beam distribution at QD1 is peaked [Figs. 19(a) and 19(c)], we define these measurements to represent the initial perturbation of the density profile (mainly to a radial $n = 2$ mode; a fuller description of the perturbation is composed of additional higher order eigenmodes). Then, the difference in the density profiles at the exit of the transport section (D2) is interpreted as the difference in the phase of the perturbation. At respective tune depressions $\frac{\nu}{\nu_0} = 0.19$ and 0.16 for the 60% and 80% fill factor cases, the phase difference expected at D2 (five lattice periods downstream) is $\Delta\phi = 167°$. Since the beam distribution started peaked at QD1 for both cases, we expect the distribution to be almost completely out of phase at D2 [Figs. 19(b) and 19(d)]. An additional 20–30 quadrupoles would increase the transport length to 4.5–6 times $(2\pi\nu/\omega_p)$ plasma periods, and theoretical models predict that this would be just enough for the space-charge waves to phase mix, eliminating most of the phase-space and distribution inhomogeneities [35,37,44].

Crossed-slit current density profile data prompted a comparison to an idealized thermal equilibrium distribution using the Vlasov equation, which showed that the equivalent thermal distribution profile falls rapidly at the beam edge in 5 Debye lengths (95% to 5%), $\lambda_{Dx,y}$, outside a near-constant density core, with

$$\lambda_{Dx} = \frac{\varepsilon_x}{2}\sqrt{\frac{b}{2K\gamma_b^2 a}}, \tag{8a}$$

$$\lambda_{Dy} = \frac{\varepsilon_y}{2}\sqrt{\frac{a}{2K\gamma_b^2 b}}, \tag{8b}$$

where $\gamma_b = 1$ is the Lorentz factor of the beam. For the HCX beam parameters, $\lambda_{Dx} \approx 0.8$–0.9 mm (80%–60% fill factor) and $\lambda_{Dy} \approx 0.4$–0.7 mm (60%–80% fill factor). Thus, the rate of falloff calculated is in reasonable agreement with the data ($\sim$ 2–5 mm) and measured beam emittance, though the actual beam is not in thermal equilibrium. The beam temperature is not the same in both projection planes due to the different beam sizes, so the model predicts that the rate of the beam edge falloff should be steeper in the vertical (y) direction (diverging, colder at all measurement planes) than in the horizontal (x) direction (converging, warmer at all measurement planes). However, because of the 1 mm x and y spatial resolution of our current density maps, the relatively small difference was not resolved. Moreover, a more quantitative interpretation of the data requires including the effects of dynamics induced halo and space-charge waves.

Transport experiments in the magnetic quadrupole section have started, with a focus on developing new *in situ* diagnostics to measure (directly or indirectly) quantities such as the degree of beam neutralization, the electron and neutral density, and the beam potential radial distribution. Measurements in the magnetic transport section will also have a direct impact on the design of future heavy-ion induction accelerators. In future publications, comparisons will be made between the experiments and theories of electron dynamics in magnets [26,54]. In parallel, superconducting quadrupoles and compact cryostats are being designed and tested [55] for similar experiments on the HCX beam line.

In order to develop the capability to simulate intense beams for accelerator design, details of the measured phase-space distribution are being used to initialize particle-in-cell simulations for comparison of data with theoretical models. Prototype diagnostics with scintillator imaging show that the higher data acquisition rates and measurement of all the correlations in the four-dimensional transverse phase space available with this diagnostic will enhance the theory/experiment comparison.

The measurement of the head and tail energy variations with respect to the core of the beam pulse was used to help

complete the design of a bunch end control module [56] (an induction module to correct the energy versus time profile of the bunch) to be installed between the matching section and the periodic transport lattice. It is designed to correct ± 20 kV waveform imperfections and also provides 100–200 kV longitudinal focusing voltages to counteract the longitudinal space-charge field at the head and tail of the beam. Experiments with this module will be a first step towards conducting longitudinal physics experiments on a longer transport lattice.

Higher fill factors will also be studied. For an induction linac driver composed of many (~ 100) parallel beams that should be nearly identical, there will be additional system complexity, with some alignment and matching issues that have not been addressed explicitly in this experiment. In the context of multiple-beam arrays for heavy-ion fusion, electrostatic quadrupoles composed of cylindrical electrodes make a compact unit cell. For the 1-MeV beam measurements, the current density averaged over a unit cell is $\langle J \rangle \approx 40\ \mathrm{A\,m^{-2}}$ (denominator includes the area occupied by the beam focusing electrodes between adjacent channels of an array), and future measurements at 1.8 MeV will increase this by a factor of 2.4, to nearly $100\ \mathrm{A\,m^{-2}}$.

Designing a future linear accelerator for heavy-ion fusion on the basis of the 60%–80% fill factor would constitute a significant departure from other linear accelerators, which rarely exceed 50% (at 2σ) in order to accommodate the tail of the Gaussian beam distributions. For example, the SNS linac [4,57] or Rare Isotope Accelerator [58–60] have design fill factors in the range of 30%–55%, and the maximum fill factor only occurs over short regions in the lattice. Most of a fusion driver will use magnetic quadrupole focusing, which has increased strength at higher ion velocity than electrostatic quadrupoles. Though the field quality of magnetic [55] and electrostatic lattices may be similar in an integrated sense, field nonlinearities are different in spatial distribution at the lead and return ends. The useful fill factor in the magnetic lattice will also be influenced by trapped secondary electrons [61], and gas desorption. The influence of gas desorption is mitigated by shorter pulse length at higher ion kinetic energy.

There is a design trade-off between (a) the frequency of diagnostics, steering and matching adjustments, (b) manufacturing and alignment tolerances, and (c) fill factor. A higher fill factor will generally require more frequent beam adjustments. In particular, the difficulties we encountered in controlling the beam centroid motion emphasize the importance of measuring and correcting for beam centroid displacements. However, the 80% fill factor results together with additional observations made for misaligned beams at the entrance of the electrostatic transport section (Sec. VI) suggest that correction elements may only be needed every ten lattice periods (20 quads, 4.4 m). Note that the beam centroid oscillations are driven by the applied strength of the focusing element, which in our experiment produced $\sigma_0 < 70°$. A fusion driver would probably operate at $\sigma_0 \approx 80°$, making it more sensitive to misalignment errors and centroid offsets.

The calculated maximum envelope excursion is expected to grow by about 0.1 mm per five lattice periods (Sec. VI). This result implies that, for RMS envelope control, beam rematching is not critical for the transport of high fill factor beams over long (50 lattice periods) distances. However, these extrapolations do not address the magnitude of emittance growth and halo formation due to mismatch over long distances.

X. CONCLUSION

The High Current Experiment studies—at driver-relevant parameters—the question of how much clearance is needed to transport high-line-charge-density, high-perveance beams over long distances with acceptable beam degradation, and from this to also refine the value of the channel size for the transport of the maximum charge averaged over an array of beams. This is important input for the future design of a heavy-ion fusion driver.

We successfully improved the optics of the 2-MV injector to deliver a beam compatible with the experiments downstream, with reduced emittance and reduced phase-space distortions. While the current density distribution remains nonideal, the final normalized emittance is low ($< 0.5\pi$ mm mrad for 180 mA at the exit of the matching section).

The achievable beam envelope and centroid control in the matching section are key ingredients in determining the allowable fill factor in the downstream transport channel. We find that the large transverse compression factors of the matching section result in greater sensitivity to the fringe field of the optics. Even though it often required several iterations, the required beam control was successfully achieved, with <1.5 mm mismatch amplitudes in the downstream channel.

The results of transport through the first ten electrostatic quadrupoles indicate transport with a high beam fill factor (at least 80%) is possible with negligible emittance growth and beam loss. This was achieved in a single beam line that includes most of the uncertainties that surround the construction of a full-scale driver (e.g., manufacturing of components, system alignment, high-voltage stability) and the production of a high current beam (current density nonuniformities, velocity tilt, halo particles, partial neutralization) except for the uncertainties related to an array configuration.

Accurately modeling effects such as the behavior of halo and secondary particles that result from interactions with the wall or the background gas and the detailed beam current distribution is where present theoretical and computational efforts are focused. While 10 or 20 quadrupoles are too few for settling questions of emittance evolution in a long transport system, they are of the correct length for

the rapid initial evolution of the emittance and beam profile, which is expected in the front end of an accelerator. System studies show that the cost dependence of a fusion power plant with respect to the fill factor makes high fill factors very desirable [18]. PIC simulations initialized with a semi-Gaussian distribution indicate that 80% might be a limit of what is achievable [35] and is near the threshold for particle loss from halo formation.

Agreement within experimental and model uncertainties was reached between an improved envelope model of the transport section and the data. More precise models of the beam dynamics will include image charge forces and applied field nonlinearities, which influence the envelope excursions. The modeling of these effects is being pursued in ongoing PIC simulations. In addition, measurements of the beam current density distribution at the entrance and exit of the transport section and TOF measurements showed good agreement with simple theories describing the transverse and longitudinal evolution of the space charge of the beam, respectively (i.e., space-charge waves).

Image charge forces in the transport section do not cause significant distortions of the beam's transverse distribution. In particular, the diamondlike shape of the current density distribution and the "hooks" seen in the phase-space distribution at the exit of the matching section are not enhanced in the transport section. These distortions are believed to be due to rapid envelope transitions in the matching section. A detailed understanding of the phase-space distribution awaits a better model of the matching section fields and PIC simulations.

Beam stability (i.e., envelope parameter variations) throughout the pulse was significantly improved by flattening the beam current waveform, therefore proving that the earlier behavior (i.e., large envelope variations throughout the beam pulse) was not due to a buildup of charge resulting from the beam propagating through the background gas.

First halo measurements showed that within the sensitivity of the present diagnostics (10^{-3}), the beam does not extent farther than 5 mm from the steep edge of the core density.

Finally, the beam energy distribution was measured and is consistent with earlier measurements [36], where the head was found to be accelerated and the tail decelerated with respect to the flattop of the beam. This effect is due to the longitudinal space charge of the beam.

Future plans include a long transport experiment with $\approx$ 100 quadrupoles such as described in Refs. [62–64], designed to explore transverse phase-space dynamics as well as longitudinal phase-space dynamics during compression and final focusing, integrating for the first time several beam physics manipulations required in a fusion driver. It is a necessary step to develop and demonstrate integrated modeling capabilities of all significant beam manipulations from source to target.

ACKNOWLEDGMENTS

The authors gratefully acknowledge the outstanding technical support of the LBNL mechanical and electrical teams led by Mr. R. Hipple and Mr. W. Strelo. I. Haber (University of Maryland), J.-L. Vay (LBNL), E. Lee (LBNL), and J. Barnard (LLNL) also provided support and insight to the beam physics. The support of R. Bangerter and G. Logan is gratefully acknowledged. This work was performed under the auspices of the U.S. Department of Energy by University of California, Lawrence Livermore and Lawrence Berkeley National Laboratories, under Contracts No. W-7405-Eng-48 and No. DE-AC03-76SF00098

APPENDIX

The statistical beam envelope radii and angles are defined as

$$a = 2\sqrt{\langle (x - \langle x\rangle)^2\rangle}, \tag{A1a}$$

$$a' = \frac{2\langle (x - \langle x\rangle)\cdot(x' - \langle x'\rangle)\rangle}{\sqrt{\langle (x - \langle x\rangle)^2\rangle}}, \tag{A1b}$$

$$b = 2\sqrt{\langle (y - \langle y\rangle)^2\rangle}, \tag{A1c}$$

$$b' = \frac{2\langle (y - \langle y\rangle)\cdot(y' - \langle y'\rangle)\rangle}{\sqrt{\langle (y - \langle y\rangle)^2\rangle}}, \tag{A1d}$$

where $\langle\ \rangle$ denotes a transverse statistical average over the beam distribution. Throughout this paper, the envelope parameters a, a', b, and b' calculated according to Eqs. (A1) from the data acquired with our slit scanners are employed. The factor of 2 in the averages ensures that a and b correspond to edge radii of an ideal uniform-density beam of elliptical cross section. These definitions are also consistent with the perimeter of an ideal K-V distribution [65].

The horizontal statistical RMS emittance is defined from the second moments of the beam:

$$\varepsilon_{x,\mathrm{RMS}} = \sqrt{\langle (x-\langle x\rangle)^2\rangle\cdot\langle (x'-\langle x'\rangle)^2\rangle - \langle (x-\langle x\rangle)\cdot(x'-\langle x'\rangle)\rangle^2}, \tag{A2}$$

and similarly for the vertical (y) direction.

[1] P. A. Seidl *et al.*, in *Proceedings of the 2001 Particle Accelerator Conference, Chicago, IL, 2001*, edited by Peter Lucas and Sara Webber (IEEE, Piscataway, NJ, 2001), p. 2932, http://accelconf.web.cern.ch/accelconf/p01/PAPERS/RPAH037.PDF

[2] R. O. Bangerter, Philos. Trans. R. Soc. London A **357**, 575 (1999).

[3] R. O. Bangerter, Nucl. Instrum. Methods Phys. Res., Sect. A **464**, 17 (2001).

[4] M. White, in *Proceedings of the XXI International Linac Conference, Gyeongju, Korea, 2002* (Pohang Accelerator Laboratory, Gyeongju, Korea, 2002), p. 1, http://accel-conf.web.cern.ch/ accelconf/l02/PAPERS/MO101.PDF

[5] A. Ratti *et al.*, in *Proceedings of the XXI International Linac Conference, Gyeongju, Korea, 2002* (Ref. [4]), p. 509, http://accelconf.web.cern.ch/ accelconf/l02/ PAPERS/TU483.PDF

[6] U.S. Department of Energy, Office of Science, Report No. SNS-100000000-PL0001-R10, 2003, http: // www.sns.gov/documentation/100000000-PL0001-R09.pdf

[7] C. Johnstone *et al.*, in *Proceedings of the 1995 Particle Accelerator Conference, Dallas, 1995* (IEEE, Piscataway, NJ, 1995), p. 86.

[8] D. Errede *et al.*, in *Proceedings of the 2003 Particle Accelerator Conference, Portland, OR, 2003*, edited by Joe Chew, Peter Lucas, and Sara Webber (IEEE, Piscataway, NJ, 2003), p. 983, http://accelconf.web.-cern.ch/accelconf/p03/PAPERS/MPPB078.PDF

[9] D. E. Young, V. Dudnikov, M. Popovic, C. W. Schmidt, and D. Sun, in *Proceedings of the 2001 Particle Accelerator Conference, Chicago, IL, 2001* (Ref. [1]), p. 3915, http://accelconf.web.cern.ch/accelconf/p01/ PAPERS/FPAH102.PDF

[10] S. S. Yu *et al.*, Fusion Sci. Technol. **44**, 266 (2003).

[11] W. M. Fawley *et al.*, Phys. Plasmas **4**, 880 (1997).

[12] M. G. Tiefenback and D. Keefe, IEEE Trans. Nucl. Sci. **32**, 2483 (1985).

[13] P. A. Seidl, C. M. Celata, A. Faltens, E. Henestroza, and S. A. McLaren, Phys. Rev. ST Accel. Beams **6**, 090101 (2003).

[14] S. A. MacLaren, A. Faltens, P. A. Seidl, and D. V. Rose, Phys. Plasmas **9**, 1712 (2002).

[15] M. G. Tiefenback, Ph.D. thesis, University of California, Berkeley, 1986.

[16] http://www.ipr.umd.edu/ebte/ring/

[17] S. Bernal *et al.*, in *Proceedings of the 2003 Particle Accelerator Conference, Portland, OR, 2003* (Ref. [8]), p. 426, http://accelconf.web.cern.ch/accelconf/ p03/PAPERS/WOAC006.PDF

[18] Wayne Meier (private communication).

[19] W. Abraham *et al.*, in *Proceedings of the 1995 Particle Accelerator Conference, Dallas, 1995* (Ref. [7]), p. 902.

[20] S. Yu *et al.*, in *Proceedings of the 1993 Particle Accelerator Conference, Washington, D.C., 1993*, edited by S. T. Corneliussen (IEEE, Piscataway, NJ, 1993), p. 703, http://accelconf.web.cern.ch/accelconf/p93/PDF/ PAC1993_0703.PDF

[21] F. M. Bieniosek, E. Henestroza, J. W. Kwan, L. Prost, and P. Seidl, in *Proceedings of the 2001 Particle Accelerator Conference, Chicago, IL, 2001* (Ref. [1]), p. 2099, http:// accelconf.web.cern.ch/accelconf/p01/PAPERS/ WPAH011.PDF

[22] J. W. Kwan, F. M. Bieniosek, E. Henestroza, L. Prost, and P. Seidl, Laser Part. Beams **20**, 441 (2002).

[23] S. McLaren, Ph.D. thesis, University of California, Berkeley, 2000.

[24] F. Bieniosek, J. Kwan, L. Prost, and P. Seidl, Rev. Sci. Instrum. **73**, 2867 (2002).

[25] The Mathworks, Inc., Natick, MA 01760, http:// www.mathworks.com

[26] A. W. Molvik *et al.*, in *Proceedings of the 2003 Particle Accelerator Conference, Portland, OR, 2003* (Ref. [8]), p. 312, http://accelconf.web.cern.ch/accelconf/ p03/PAPERS/TOPC004.PDF

[27] F. M. Bieniosek, L. Prost, and W. Ghiorso, in *Proceedings of the 2003 Particle Accelerator Conference, Portland, OR, 2003* (Ref. [8]), p. 2524, http://accelconf.web.cern.ch/ accelconf/p03/PAPERS/WPPB050.PDF

[28] R. C. Dehmel, H. K. Chau, and H. H. Fleischmann, Atomic Data **5**, 231 (1973).

[29] D. P. Grote, A. Friedman, I. Haber, W. Fawley, and J.-L. Vay, Nucl. Instrum. Methods Phys. Res., Sect. A **415**, 428 (1998).

[30] A. Friedman, D. P. Grote, and I. Haber, Phys. Fluids B **4**, 2203 (1992).

[31] D. P. Grote and A. Friedman, Part. Accel. **37–38**, 141 (1992).

[32] R. W. Hockney and J. W. Eastwood, *Computer Simulation using Particles* (McGraw-Hill, New York, 1981), p. 215.

[33] David P. Grote, WARP Manual, 1998, Lawrence Livermore National Laboratory, 7000 East Avenue, Livermore, CA 94550-9234, USA.

[34] Zane Mottler, Lee Busby, and Fred N. Fritsch, *The Python Graphics Interface, Part IV: Python Gist Graphics Manual*, Lawrence Livermore National Laboratory Report No. UCRL-MA-128569, Manual 4, 1998.

[35] C. M. Celata, D. P. Grote, and I. Haber, Laser Part. Beams **20**, 577 (2002).

[36] S. S. Yu *et al.*, in *Proceedings of International Symposium on Heavy Ion Inertial Fusion, Princeton, 1996*, edited by J. J. Barnard, T. J. Fessenden, and E. P. Lee (PPPL, Princeton, NJ, 1996), p. 309.

[37] S. M. Lund, J. J. Barnard, and E. P. Lee, in *Proceedings of the XX International Linac Conference, Monterey, CA, 2000*, edited by A. W. Chao (SLAC, Stanford, CA, 2000), p. 290, http://accelconf.web.cern.ch/accelconf/l00/ papers/MOE11.pdf

[38] Martin Reiser, *Theory and Design of Charged Particle Beams* (Wiley, New York, 1994), pp. 240–252.

[39] R. C. Davidson, *Physics of Nonneutral Plasmas* (Addison-Wesley, Reading, MA, 1990), pp. 171–177.

[40] T. P. Wangler, K. R. Crandall, R. S. Mills, and M. Reiser, IEEE Trans. Nucl. Sci. **32**, 2196 (1985).

[41] J. R. Pierce, *Theory and Design of Electron Beams* (Van Nostrand, Princeton, 1949).

[42] F. M. Bieniosek *et al.*, Phys. Rev. ST Accel. Beams **8**, 010101 (2005).

[43] D. Baca, J. W. Kwan, J. K. Wu, and E. Chacon-Golcher, in *Proceedings of the 2003 Particle Accelerator Conference, Portland, OR, 2003* (Ref. [8]), p. 3294, http://accelconf.-web.cern.ch/accelconf/p03/PAPERS/FPAB005.PDF

[44] A. Friedman *et al.*, in *Proceedings of the 2003 Particle Accelerator Conference, Portland, OR, 2003* (Ref. [8]), p. 275, http://accelconf.web.cern.ch/accelconf/ p03/PAPERS/TOPB006.PDF

[45] C. M. Celata *et al.*, in *Proceedings of the 2003 Particle Accelerator Conference, Portland, OR, 2003*

(Ref. [8]), p. 1518, http://accelconf.web.cern.ch/accelconf/p03/PAPERS/TPAG039.PDF

[46] S. M. Lund and B. Bukh, Phys. Rev. ST Accel. Beams **7**, 064201 (2004).

[47] S. M. Lund *et al.*, Nucl. Instrum. Methods Phys. Res., Sect. A **415**, 345 (1998).

[48] R. L. Gluckstern, in *Proceedings of the 1970 Proton Linear Accelerator Conference, Batavia, IL, 1971*, edited by R. M. Tracy (National Accelerator Laboratory, Batavia, 1971), p. 811.

[49] L. I. Hofmann, L. J. Laslett, L. Smith, and I. Haber, Part. Accel. **13**, 145 (1983).

[50] M. Lampel and M. Tiefenback, Appl. Phys. Lett. **43**, 57 (1983).

[51] J.-L. Vay *et al.*, Phys. Plasmas **11**, 2928 (2004).

[52] S. M. Lund and B. Bukh, Phys. Rev. ST Accel. Beams **7**, 024801 (2004).

[53] S. M. Lund and R. C. Davidson, Phys. Plasmas **5**, 3028 (1998).

[54] A. W. Molvik *et al.*, in *Proceedings of the 31st ICFA Advanced Beam Dynamics Workshop on Electron-Cloud Effects (ECLOUD'04), Napa, CA, 2004* (CERN Report No. 2005-001, 2005).

[55] G. L. Sabbi *et al.*, in *Proceedings of the 2003 Particle Accelerator Conference, Portland, OR, 2003* (Ref. [8]), p. 1990, http://accelconf.web.cern.ch/accelconf/p03/PAPERS/WPAE023.PDF

[56] C. Burkhart, U.S. Department of Energy SBIR Final Report No. DE-FG03-00ER83010, 2001.

[57] D. Jeon, in *Proceedings of the 2003 Particle Accelerator Conference, Portland, OR, 2003* (Ref. [8]), p. 107, http://accelconf.web.cern.ch/accelconf/p03/PAPERS/TOAA003.PDF

[58] R. C. York, *Radiochemistry at RIA Symposium in conjunction with the 225th ACS National Meeting, New Orleans, LA, 2003*, http://www.cem.msu.edu/~mantica/radio-ria/york_radioria.pdf

[59] P. N. Ostroumov *et al.*, Phys. Rev. ST Accel. Beams **5**, 060101 (2002).

[60] X. Wu *et al.*, in *Proceedings of the XXI International Linac Conference, Gyeongju, Korea, 2002* (Ref. [4]), p. 133, http://accelconf.web.cern.ch/ accelconf/l02/PAPERS/MO441.PDF

[61] R. Cohen *et al.*, in *Proceedings of the 2003 Particle Accelerator Conference, Portland, OR, 2003* (Ref. [8]), p. 132, http://accelconf.web.cern.ch/accelconf/p03/PAPERS/TOAA010.PDF

[62] M. A. Leitner *et al.*, in *Proceedings of the 2003 Particle Accelerator Conference, Portland, OR, 2003* (Ref. [8]), p. 1521, http://accelconf.web.cern.ch/accelconf/p03/PAPERS/TPAG040.PDF

[63] J. J. Barnard *et al.*, Laser Part. Beams **21**, 553 (2003).

[64] C. M. Celata *et al.*, in *Proceedings of the Third International Conference on Inertial Fusion Sciences and Applications (IFSA 2003), Monterey, CA*, edited by B. A. Hammel, D. D. Meyerhofer, J. Meyer-ter-Vehn, and H. Azechi (ANS, La Grange Park, IL, 2004).

[65] I. M. Kapchinsky and V. V. Vladimirsky, in *Proceedings of the 1959 International Conference on High Energy Accelerators, Geneva, 1959* (CERN, Geneva, 1959), p. 274.